

A pathogen-derived metabolite induces microglial activation via odorant receptors

NaHye Lee^{1,2} , YoonGyu Jae^{1,2} , Minhyung Kim³, TaeHo Cho¹, ChaeEun Lee¹, Yu Ri Hong¹, Do Young Hyeon³, Sanghyun Ahn³, Hongmok Kwon⁴, Kyul Kim⁴, Jae Hoon Jung³, Sehyun Chae³, Jeong-Oh Shin⁵, Jinwoong Bok⁵, Youngjoo Byun⁴ , Daehee Hwang^{3,6} and JaeHyung Koo¹ 

- 1 Department of New Biology, DGIST, Daegu, Korea
- 2 Department of Brain and Cognitive Sciences, DGIST, Daegu, Korea
- 3 Center for Plant Aging Research, DGIST, Daegu, Korea
- 4 College of Pharmacy, Korea University, Sejong, Korea
- 5 Department of Anatomy, Yonsei University College of Medicine, Seoul, Korea
- 6 Department of Biological Sciences, Seoul National University, Korea

Keywords

microglial activation; non-olfactory expression; odorant receptor; pathogenic metabolite

Correspondence

J. Koo, Department of New Biology, DGIST, Daegu 42988, Korea

Tel: +82-53-785-6112

E-mail: jkoo001@dgist.ac.kr

D. Hwang, Department of Biological Sciences, Seoul National University, Seoul 08826, Korea

Tel: +82-2-880-7522

E-mail: daehee@snu.ac.kr

NaHye Lee and YoonGyu Jae equally contributed to this work

(Received 17 September 2019, revised 10 December 2019, accepted 27 January 2020)

Abbreviations

2-PF, 2-pentylfuran; 5x FAD, familial Alzheimer's disease; AC, Adenylyl cyclase; aCSF, artificial cerebrospinal fluid; AD, Alzheimer's disease; Akt, protein kinase B; APP/PS1, Amyloid precursor protein/presenilin 1; AS, astrocytes; BLAST, Basic Local Alignment Search Tool; cAMP, cyclic adenosine monophosphate; CNS, central nervous system; CREB, cAMP response element-binding protein; DAPI, 4',6-diamidino-2-phenylindole; DCF-DA, 2',7'-dichlorodihydrofluorescein diacetate; DEGs, differentially expressed genes; DMEM, Dulbecco's modified Eagle's medium; EIC, extracted ion chromatogram; Endo, endothelial cells; ERK, extracellular signal-regulated kinase; FACS, fluorescence-activated cell sorting; FITC, fluorescein isothiocyanate; FPKM, fragment per kilobase per million; FT, flow-through; GFAP, glial fibrillary acidic protein; GOBPs, gene ontology biological processes; GPCRs, G protein-coupled receptors; HESI, heated electrospray ionization; HMDB, human metabolome database; IHC, immunohistochemistry; JNK, c-Jun N-terminal kinase; LC-MS/MS, liquid chromatography–tandem mass spectrometry; LPS, lipopolysaccharides; M.W., molecular weight; MAPK, mitogen-activated protein kinase; MFI, mean fluorescence intensity; MG, microglia; MO, myelinating oligodendrocytes; MOI, multiplicity of infection; MOR, mouse olfactory receptor; MS/MS, tandem mass spectrometry; NCBI, National Center for Biotechnology Information; Neu, neurons; NFO, newly formed oligodendrocytes; OPC, oligodendrocyte precursor cells; ORs, odorant receptors; PDB, protein data bank; PI3K, phosphoinositide 3-kinases; PKA, protein kinase A; PLC, phospholipase C; PRRs, pattern recognition receptors; qRT-PCR, quantitative real-time polymerase chain reaction; ROS, reactive oxygen species; RTP1S, receptor-transporting protein 1S; SEM, standard error of the mean; *Streptococcus pneumoniae*, *S. pneumoniae*; Sup, *S. pneumoniae* culture supernatants.

Microglia (MG), the principal neuroimmune sentinels in the brain, continuously sense changes in their environment and respond to invading pathogens, toxins, and cellular debris, thereby affecting neuroinflammation. Microbial pathogens produce small metabolites that influence neuroinflammation, but the molecular mechanisms that determine whether pathogen-derived small metabolites affect microglial activation of neuroinflammation remain to be elucidated. We hypothesized that odorant receptors (ORs), the largest subfamily of G protein-coupled receptors, are involved in microglial activation by pathogen-derived small metabolites. We found that MG express high levels of two mouse ORs, Olfr110 and Olfr111, which recognize a pathogenic metabolite, 2-pentylfuran, secreted by *Streptococcus pneumoniae*. These interactions activate MG to engage in chemotaxis, cytokine production, phagocytosis, and reactive oxygen species generation. These effects were mediated through the G_{αs}-cyclic adenosine monophosphate–protein kinase A–extracellular signal-regulated kinase and G_{βγ}-phospholipase C–Ca²⁺ pathways. Taken together, our results reveal a novel interplay between the pathogen-derived metabolite and ORs, which has major implications for our understanding of microglial activation by pathogen recognition.

doi:10.1111/febs.15234

Database

Model data are available in the PMDB database under the accession number PM0082389.

Introduction

Microglia (MG), the resident innate immune cells in the central nervous system (CNS), play important roles in coordinating the defense against infection by pathogens [1,2]. After infection, MG are rapidly activated in a manner that depends on substances released from the pathogen, resulting in morphological changes, chemotaxis, cytokine production, phagocytosis, and reactive oxygen species (ROS) generation [3]. MG are activated after the recognition of large pathogen-associated molecular patterns [lipopolysaccharides (LPS), glycans, flagellin, etc.] by their cognate pattern recognition receptors (PRRs) [4]. For example, *Streptococcus pneumoniae* is the most common causative pathogen of meningitis, and microglial activation characterizes brain inflammatory responses following *S. pneumoniae* infection [5,6]. Several large molecules, including pneumolysin [7,8], pneumococcal surface protein C [9], and cell wall components, can induce microglial activation [10]. However, it remains relatively unclear whether small metabolites derived from pathogens can also serve as molecular patterns capable of activating MG.

Odorant receptor (ORs) are the largest subfamily of G protein-coupled receptors (GPCRs), accounting for 50% of GPCRs (388 ORs) in humans and 61% of GPCRs (1037 ORs) in mice [11]. MG express diverse GPCRs that sense both large and small molecules [12,13]. Some GPCRs sense small metabolites and affect microglial activation [14,15], but to date no ORs have been shown to recognize pathogen-derived metabolites in MG. ORs can detect small metabolites in a variety of peripheral tissues, such as kidney, skin, and pancreatic tissues beyond the nose [16–19]. For example, recognition of a sandalwood odorant by OR2AT4 promotes the proliferation of keratinocytes in human skin, which induces wound healing [20]. Olfr78 also recognizes small-chain fatty acids in the renal juxtaglomerular apparatus, which helps to regulate renin secretion and blood pressure [16]. Collectively, these data are consistent with the idea that ORs serve as receptors for metabolites in many tissues and cell types. We hypothesized that small metabolites from pathogens can activate MG via ORs in peripheral tissues, as well as in the CNS.

ORs expressed in nonolfactory tissues of the body [17,18] are called ectopic ORs [21] or chemosensory

GPCRs [22]. They appear to have biological functions beyond smell perception, similar to those of common GPCRs. Several of these ectopic ORs have been reported to be dysregulated in association with brain disorders such as Alzheimer's disease (AD), Parkinson's disease, and schizophrenia [23], both in the human diseases and in mouse models of these disorders. For example, some ORs are abnormally regulated in the dorsolateral prefrontal cortex of schizophrenia patients [24], cerebral cortex of AD-associated Amyloid precursor protein/presenilin 1 (APP/PS1) or familial Alzheimer's disease (5× FAD) transgenic animal models [25,26], and mesencephalic dopaminergic neurons associated with several neurodegenerative and psychiatric disorders [27]. Despite an increased research focus on OR expression in normal and pathological brains, little is known about the ligands and pathophysiological roles of brain ORs, and their molecular mechanisms remain to be elucidated.

In this study, we sought to determine whether small metabolites secreted by *S. pneumoniae* induce microglial activation, and if so, which mediators are involved. To address these questions, we investigated whether small metabolites from *S. pneumoniae* culture supernatants could induce microglial activation. Using multiple approaches, including RNA-sequencing, OR-metabolite screening, molecular modeling, and site-directed mutagenesis, we specifically deorphanized two microglial ORs, Olfr110 and its homologue Olfr111, with 2-pentylfuran (2-PF) as a ligand. Intriguingly, we detected 2-PF by LC-MS/MS in culture supernatants of *S. pneumoniae*, which induce microglial activation. Furthermore, we showed that the 2-PF–Olfr110 interaction is specifically involved in microglial activation *in vitro* and *ex vivo*. Finally, we demonstrated that microglial activation evoked by 2-PF–Olfr110 is mediated by a combination of the $G_{\alpha s}$ –cyclic adenosine monophosphate(cAMP)–protein kinase A (PKA)–extracellular signal-regulated kinase (ERK) and $G_{\beta\gamma}$ –phospholipase C (PLC)– Ca^{2+} pathways. Based on our observations, we conclude that microglial Olfr110 and Olfr111 act as the receptors for 2-PF, a small metabolite from *S. pneumoniae*, enabling MG to sense pathogen infection and induce microglial activation.

Results

Secreted metabolites from *S. pneumoniae* induce microglial activation

First, we investigated whether *S. pneumoniae* culture supernatants (Sup) can activate both MG and astrocytes (AS) by measuring cytokine secretion. MG and AS release pro- and anti-inflammatory cytokines after infection [28]. Therefore, we sought to determine which cell type was primarily responsible for the increase in cytokine secretion after treatment of primary MG and AS with Sup. Surprisingly, mRNA expression levels of all five cytokines (*Tnf*, *Il6*, *Il1b*, *Il10*, and *Il13*) increased significantly ($P < 0.001$) in Sup-treated MG, but not in Sup-treated AS (Fig. 1A). We also observed dose-dependent increases in the levels of cytokine proteins (TNF- α , IL6, and IL1b) in primary MG (Fig. 1B). We also measured three other features of microglial activation: chemotaxis, ROS (O_2^-) generation, and phagocytosis. All of these features were significantly induced ($P < 0.001$) by Sup injection (Fig. 1C–E). We then filtered the Sup through Ultracel YM-3 membrane, treated primary MG with the flow-through (FT), and analyzed microglial activation. As with Sup, the FT significantly ($P < 0.001$) induced chemotaxis, ROS generation, and phagocytosis (Fig. 1F–H), suggesting that the FT contained small molecules derived from *S. pneumoniae* that induced microglial activation.

2-pentylfuran interacts with microglial Olfr110/Olfr111

We next sought to determine which receptors recognized the small-molecule ligands contained in the 3 kD membrane FT. GPCRs can sense small molecules [29,30]. ORs, the largest GPCR subfamily, are also expressed in various nonolfactory tissues [17,18], where they recognize small ligands. Hence, we hypothesized that *S. pneumoniae*-released metabolites could bind to ORs, thereby inducing microglial activation. To identify OR candidates, we performed mRNA sequencing analysis of cultured mouse (C57BL/6J) primary MG. We found that thirteen ORs (*Olfr111*, *Olfr110*, *Olfr482*, *Olfr99*, *Olfr132*, *Olfr115*, *Olfr77*, *Olfr543*, *Olfr461*, *Olfr455*, *Olfr1420*, *Olfr1417*, and *Olfr57*) were expressed in these cells, with *Olfr111* and *Olfr110* expressed at the highest levels (Fig. 2A). We further identified the candidates from a previously reported gene expression dataset (GSE52564; [31]). According to the previous data, seven ORs (*Olfr110*, *Olfr111*, *Olfr99*, *Olfr1029*, *Olfr433*, *Olfr222*, and *Olfr920*) were

expressed in MG purified using fluorescence-activated cell sorting (FACS), including *Olfr110* and *Olfr111* that are specifically expressed in purified MG relative to other brain cell types [AS, Neu, oligodendrocyte precursor cells (OPC), and endothelial cells (Endo)] (Table 1). Together, these analyses yielded 17 OR candidates.

Many receptors recognizing pathogen-associated molecular patterns are induced after pathogen infection in order to trigger effective immune responses [32]. Hence, we investigated whether these 17 OR candidates were induced in primary MG after Sup treatment using quantitative real-time polymerase chain reaction (qRT-PCR). Sup treatment up-regulated *Olfr110* and *Olfr111* to the greatest extent, followed by *Olfr920*, *Olfr1417*, and *Olfr99* (Fig. 2B). Next, we investigated whether these five candidates could react with small metabolites in Sup. For this purpose, we selected 11 small *S. pneumoniae*-derived metabolites reported in at least two independent studies (Table 2). After transient transfection of the five OR candidates, we confirmed their expression on the plasma membrane (Fig. 2C). We then assessed their reactivity with the 11 small metabolites in Hana3A cells using a luciferase assay (Fig. 2D). Among the 11 metabolites, the luciferase assay revealed that Olfr110 ($EC_{50} = 120.1$) and Olfr111 ($EC_{50} = 153.1$) specifically reacted with 2-PF (Fig. 2E; Table 3). By contrast, the other three ORs only reacted with ethanol, which we considered nonspecific because they also reacted with MOCK (Fig. 2E). Collectively, these results suggest that 2-PF could serve as a ligand for Olfr110 and Olfr111.

To further evaluate these 2-PF–OR interactions, we characterized the molecular receptive range of Olfr110 or Olfr111 with respect to 2-PF. Specifically, we compared the reactivity of nine structural analogues of 2-PF with Olfr110 or Olfr111, again using the luciferase assay. These analogues included furan, its derivatives (methyl to heptyl and t-butyl groups on the C2 position), and 2,3-dimethylfuran (Table 3). Five analogues (2-PF, 2-butylfuran, 2-t-butylfuran, 2-hexylfuran, and 2-propylfuran) exhibited reactivity with Olfr110 and Olfr111 (Fig. 3A–C). 2-PF was the most reactive, and Olfr110 exhibited stronger (1.5-fold) reactivity with 2-PF than Olfr111.

We then examined the key residues of Olfr110 for binding to 2-PF by homology modeling of Olfr110 (Table 4) and docking analysis between Olfr110 and 2-PF. Docking analysis predicted that the following amino acids of Olfr110 were important for hydrophobic interactions with 2-PF: F102 and F104 in transmembrane domain 3, and Y252 and Y259 in transmembrane domain 6 (Fig. 3D). Both F104 and

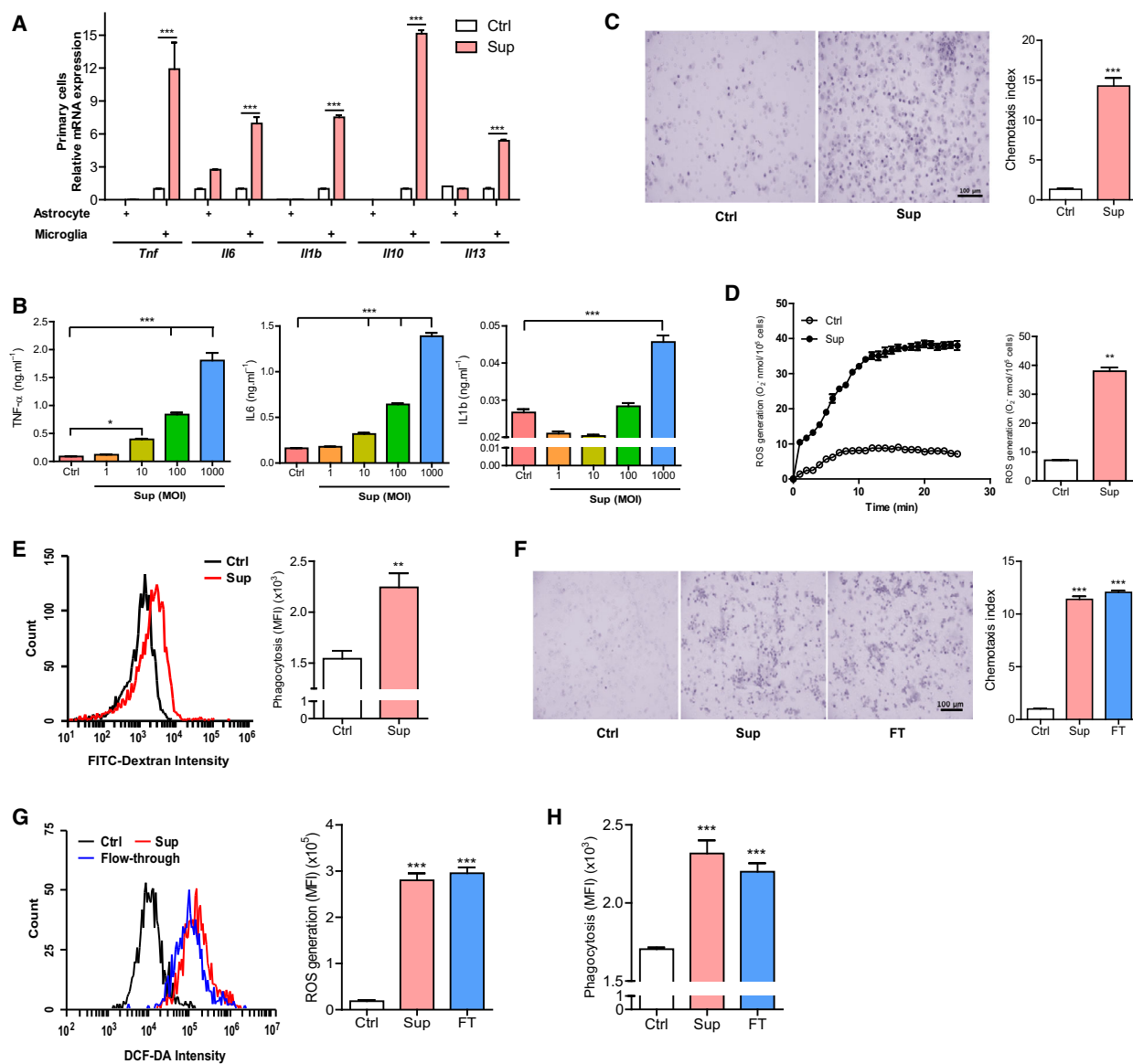


Fig. 1. Secreted metabolites from *S. pneumoniae* induce microglial activation. (A) mRNA expression levels of pro-inflammatory (*Tnf*, *Il6*, and *Il1b*) and anti-inflammatory cytokines (*Il10* and *Il13*) measured in the primary MG and AS from mouse (C57BL6/N) at 2 h after Sup treatment ($n = 3/\text{condition}$, $P < 0.001$ by one-way ANOVA with Tukey's *post hoc* correction). (B) Protein levels of cytokines (TNF- α , IL6, and IL1b) measured from primary MG at 24 h after treatment with Sup containing four different doses of *S. pneumoniae* (multiplicity of infection [MOI] of 1, 10, 100, and 1000; $n = 3/\text{condition}$, $*P < 0.05$, $**P < 0.01$ and $***P < 0.001$ by one-way ANOVA with Student's *t*-test). (C) Representative images showing migration of primary MG to Ctrl or Sup for 4 h. Images were generated using the Boyden chamber assay. Chemotaxis index represents counts of migrated MG ($n = 3/\text{condition}$, $P < 0.001$ by one-way ANOVA with Tukey's *post hoc* correction). Scale bar: 100 μm . (D) Accumulated amounts of O₂⁻ generated after treatment with Ctrl or Sup, measured at 1-min intervals for 25 min. Data are means \pm SEM at each time point ($n = 3/\text{condition}$, $P < 0.01$ by one-way ANOVA with Tukey's *post hoc* correction). (E) Distribution of FITC-dextran intensities in primary MG, measured by FACS analysis after treatment with Ctrl or Sup. Phagocytosis index represents MFIs ($n = 5/\text{condition}$, $P < 0.01$ by one-way ANOVA with Tukey's *post hoc* correction). (F–H) Assays for chemotaxis ($n = 3/\text{condition}$, Scale bar: 100 μm), (F), ROS generation ($n = 5/\text{condition}$) (G), and phagocytosis ($n = 5/\text{condition}$) (H) after treatment with Ctrl, Sup, or FT. MFI measured by FACS indicate estimated amounts of ROS generation and phagocytosis. Bar charts show mean \pm SEM ($P < 0.001$ by one-way ANOVA with Student's *t*-test).

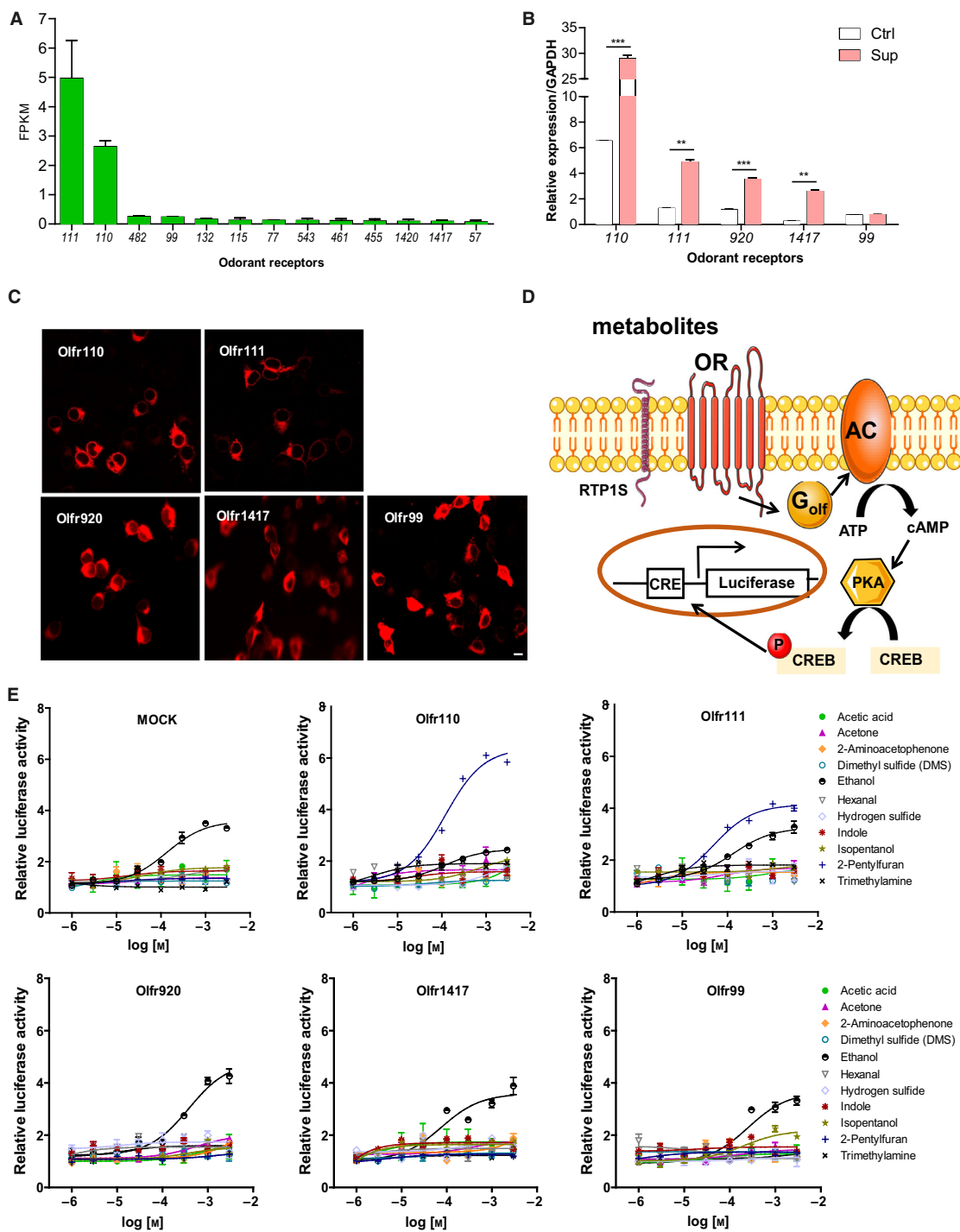


Fig. 2. Microglial Olfr110 and Olfr111 are deorphanized with 2-PF. (A) ORs expressed in primary MG, as determined by mRNA-seq data. (B) Relative expression levels of ORs induced by Sup treatment. Expression levels were normalized against GAPDH. Data in A and B are means \pm SEM ($n = 3$ /condition, $**P < 0.01$ and $***P < 0.001$ by one-way ANOVA with Student's t -test). (C) Expression of ORs on the plasma membrane of Hana3A cells. Images show immunofluorescence, representing expression of the indicated ORs. Scale bar: 40 μ m. (D) Schematic diagram illustrating the luciferase assay measuring reactivity of all possible metabolite–OR pairs in Hana3A cells. When a metabolite interacts with an OR, accumulation of cAMP is induced, thereby inducing the expression of the luciferase reporter gene via PKA and CREB. PKA, protein kinase A; cAMP response element. (E) Relative luciferase activities of Olfr110, Olfr111, Olfr920, Olfr1417, and Olfr99 vs. concentration of the indicated substrates (Table 2) containing 2-PF. MOCK: empty vector.

Table 1. Log₂-fold changes of seven ORs in MG with respect to other cell types. For example, MG/AS represents log₂-fold changes of the seven ORs in MG vs AS. MO, myelinating oligodendrocytes; and NFO, newly formed oligodendrocytes. The seven ORs were sorted in descending order of the sum of log₂-fold changes in all comparisons.

ORs	MG/AS	MG/Endo	MG/Neu	MG/OPC	MG/MO	MG/NFO	Sum
<i>Olfr110</i>	4.94	4.94	4.94	4.64	4.94	4.94	29.32
<i>Olfr111</i>	3.89	3.89	3.89	3.44	3.89	3.89	22.87
<i>Olfr99</i>	2.18	1.40	2.18	1.96	2.18	2.18	12.08
<i>Olfr1029</i>	1.13	1.13	1.13	1.13	1.13	1.13	6.79
<i>Olfr433</i>	0.51	0.51	0.51	0.51	0.51	0.51	3.06
<i>Olfr222</i>	0.49	0.49	0.49	0.49	0.49	0.49	2.94
<i>Olfr920</i>	0.14	-0.28	0.31	0.42	0.42	0.42	1.42

Y252 are important for odorant recognition by MOR256-3 [29]. We tested this prediction by performing site-directed mutagenesis of one or more of the four predicted residues (F102, F104, Y252, and Y259), and then characterized the resultant mutants by luciferase assays. Mutants with F104W mutations (F104W, F102W/F104W, F104W/Y252F/Y259F, and F102W/F104W/Y252F/Y259F) exhibited complete loss of luciferase activity, suggesting that F104 is the most critical residue for the interaction between 2-PF and Olfr110 (Fig. 3E). Chemotaxis assays revealed that after the addition of 2-PF, *Olfr110*-, or *Olfr111*-transfected cells exhibited higher levels of migration in a concentration-dependent manner (Fig. 3F). These data suggest that the 2-PF–Olfr110 interaction can alter cellular functions such as cell migration.

2-PF in *S. pneumoniae* culture supernatants induces microglial activation

Next, we investigated whether 2-PF is present in Sup by performing liquid chromatography–tandem mass spectrometry (LC-MS/MS) analysis of synthetic 2-PF, control media, and Sup. Using LC-MS/MS data obtained from synthetic 2-PF, we identified a precursor ion of 2-PF with a mass-to-charge ratio (m/z) of 153.091 (Fig. 4A,B). This precursor ion was observed in Sup, but not in control media (Fig. 4C). We observed the same MS/MS spectrum for the precursor ions in both synthetic 2-PF and Sup, suggesting that these precursor ions are identical (Fig. 4D). Next, we added 0.1 or 10 mM 2-PF to Sup and compared the intensities of the 2-PF precursor ion. The intensity was about 100-fold higher for Sup treated with 10 mM 2-PF than for Sup treated with 0.1 mM 2-PF (Fig. 4E), suggesting that 2-PF was specifically present in Sup. To determine whether 2-PF is responsible for the microglial activation induced by Sup (Fig. 1), we added 2-PF to Sup at 100, 300, and 500 μ M and then administered these samples to primary MG. Spiked

Sup significantly ($P < 0.001$) increased chemotaxis (Fig. 4F), ROS generation (Fig. 4G), and phagocytosis (Fig. 4H) in a concentration-dependent manner.

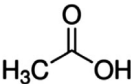
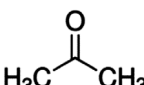
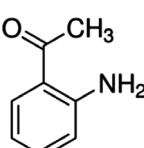
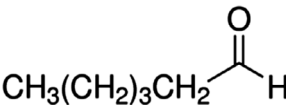
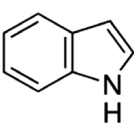
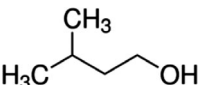
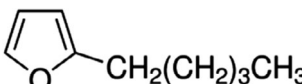
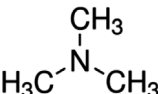
We next examined 2-PF-induced microglial activation in mouse brain. To this end, we first characterized anti-Olfr110 antibody (Table 5) using *Olfr110*-, *Olfr111*-, rat *Olr1730*-, or human *OR5V1*-transfected Hana3A cells and primary MG (Fig. 5A–C). Immunohistochemistry (IHC) with anti-Olfr110 antibody in CX3CR1-GFP transgenic mice, which express GFP in MG, showed that Olfr110 expression largely overlapped with GFP-positive cells (Fig. 5D). IHC and quantitative cell counting analysis showed strong expression of Olfr110 in Iba-1-positive MG, but not in glial fibrillary acidic protein (GFAP)-positive AS or NeuN-positive neurons of the cerebral cortex (Fig. 6A). In several brain regions, including cortex, hippocampus, hypothalamus, and substantia nigra (SN), Olfr110 was mostly expressed in Iba-1-positive MG (Fig. 6B). Furthermore, using sequential analysis followed by *in situ* hybridization for *Olfr110* transcript and IHC for Iba-1, we confirmed that *Olfr110* and Iba-1 were mainly colocalized to MG of the cerebral cortex (Fig. 6C).

Furthermore, we investigated whether 2-PF could alter *ex vivo* phagocytic activity of MG after 2-PF incubation in brain slices from CX3CR1^{GFP/+} mice. Time-lapse confocal microscopy imaging revealed that the volume, protrusions, and phagocytic activity of MG increased over time (Fig. 6D; Video S1). The number of phagocytic cells significantly ($P < 0.001$) increased, confirming increased phagocytosis (Fig. 6D). Taken together, these data suggest that 2-PF can induce microglial activation in the brain.

Olfr110 controls 2-PF-induced microglial activation

We next investigated whether 2-PF-induced microglial activation is mediated by Olfr110. For this

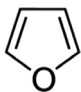
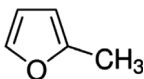
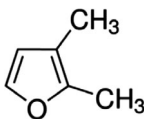
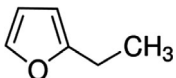
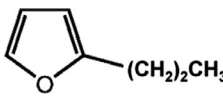
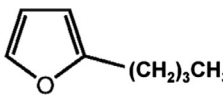
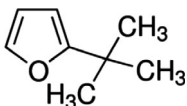
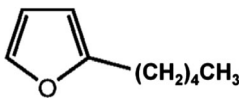
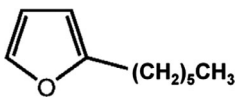
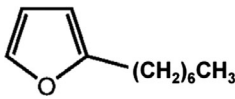
Table 2. Eleven small metabolites derived from *S. pneumoniae*. For each metabolite, the structure, metabolite name, and molecular weight (M.W.) are shown along with references to studies in which the indicated metabolite was reported.

Structure	Name	M.W.	Reference
	Acetic acid	60.05	[75,76]
	Acetone	58.08	[77,78]
	2-aminoacetophenone	135.16	[77,78]
CH ₃ SCH ₃	Dimethyl sulfide	62.43	[75,78]
CH ₃ CH ₂ OH	Ethanol	46.07	[75,78]
	Hexanal	100.16	[75,78]
H ₂ S	Hydrogen sulfide	34.08	[75,78]
	Indole	117.15	[75,78]
	Isopentanol = 3-methyl-1-butanol	88.15	[75,78]
	2-PF	138.21	[75,78]
	Trimethylamine	59.11	[75,78]

purpose, we designed specific siRNAs against Olfr110 and Olfr111, a rescue vector that restores functional Olfr110 expression. Among four siRNA candidates, we selected siRNA #3, which effectively decreased both mRNA and protein levels of Olfr110 in Hana3A cells (Fig. 7A,B). After transfection into primary MG, we observed a similar reduction in mRNA levels of Olfr110 and Olfr111 without affecting the

levels of the other ORs, negative controls (*Olfr920*, *Olfr1417*, and *Olfr99*; Fig. 7C) and in protein levels; the rescue vector abolished this effect (Fig. 7D–F). Using these siRNA #3 and rescue vector, we examined the effect of Olfr110 on 2-PF-induced microglial activation. *Olfr110* knockdown reduced the magnitude of 2-PF-induced increases in the mRNA levels of inflammatory cytokines (*Tnf*, *Il6*, *Il1b*, and *Il10*) in

Table 3. Ten furan derivatives. For each derivative, the number of carbons at the C2 position of furan, derivative name, and structure is shown, along with EC₅₀ (half-maximal effective concentration), the concentration at which reactivity reached half of the maximum reactivity in luciferase assays. N.R., no reactivity.

Number of carbons in the C2 position of furan	Name	Structure	EC ₅₀ (μM)	
			Olfr110	Olfr111
0	Furan		n.r.	n.r.
1	2-methylfuran		n.r.	n.r.
1	2,3-dimethylfuran		n.r.	n.r.
2	2-ethylfuran		n.r.	n.r.
3	2-propylfuran		100.4	120.6
4	2-butylfuran		131.2	101
4	2-t-butylfuran		131.9	110
5	2-PF		120.1	153.1
6	2-hexylfuran		521.5	94.9
7	2-heptylfuran		n.r.	n.r.

primary MG, and the rescue vector abolished the knockdown effect (Fig. 8A). We observed similar knockdown and rescue effects at the protein level

(TNF-α and IL6) in MG culture supernatants (Fig. 8B). The 2-PF-induced increase in ROS generation was reduced by the siRNAs, and this effect was

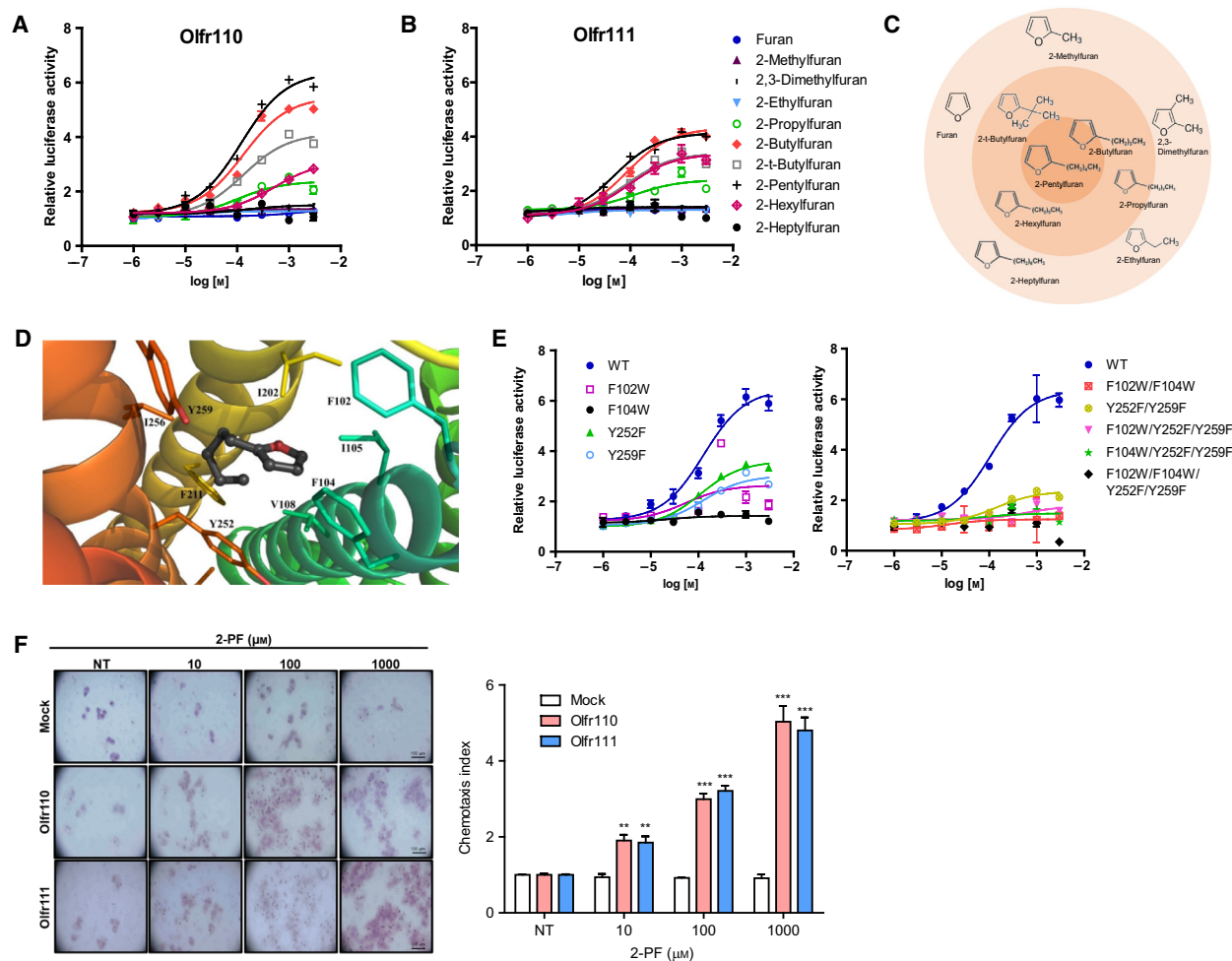


Fig. 3. 2-PF interacts with microglial Olfr110. (A–C) Relative luciferase activities of Olfr110 (A) and Olfr111 (B) vs. concentration of the indicated furan analogues (Table 3). (C) Circular map describing molecular receptive ranges of Olfr110 and Olfr111 for the 10 furan analogues used in A and B. Analogues closer to the center are more reactive. (D) Structural model of the 2-PF–Olfr110 complex showing four residues (F102, F104, Y252, and Y259) critical for the interaction between 2-PF and Olfr110. (E) Relative luciferase activities of wild-type Olfr110 and nine Olfr110 mutants vs. concentration of 2-PF. (F) Representative images showing migration of Hana3A cells expressing MOCK, Olfr110, or Olfr111 toward 2-PF. Image was generated by the Boyden chamber assay. Chemotaxis index representing counts of migrated MG was measured after treatment with control solvent (NT) or 2-PF at concentrations of 10, 100, and 1000 μM . Counts are displayed in the bar plot. Scale bar: 100 μm . Bar charts show mean \pm SEM ($n = 3$, ** $P < 0.01$ and *** $P < 0.001$ by one-way ANOVA with Tukey's *post hoc* correction).

Table 4. Results of comparative homology modeling of Olfr110 and Olfr111 via SWISS-MODEL. Sequence identity is the percentage of residues that matched exactly between two sequences. Sequence similarity is a measure estimated by SWISS-MODEL to approximate the evolutionary distance between protein sequences. Coverage of the aligned regions of protein sequences is shown.

Odorant receptor	Template protein data bank ID	X-ray structure resolution (\AA)	Sequence identity (%)	Sequence similarity	Coverage
Olfr110	3VG9	2.70	19.93	0.29	0.87
Olfr111	3VG9	2.70	20.29	0.30	0.87

reversed by the rescue vector. Notably, ATP-induced ROS generation mediated by the P2Y receptor was not affected by the siRNA or rescue vector (Fig. 8C). We observed similar 2-PF-induced effects on

phagocytosis and chemotaxis after Olfr110 knockdown and rescue (Fig. 8D,E).

We then sought to determine whether these Olfr110 knockdown and rescue effects occur in mouse brains. For

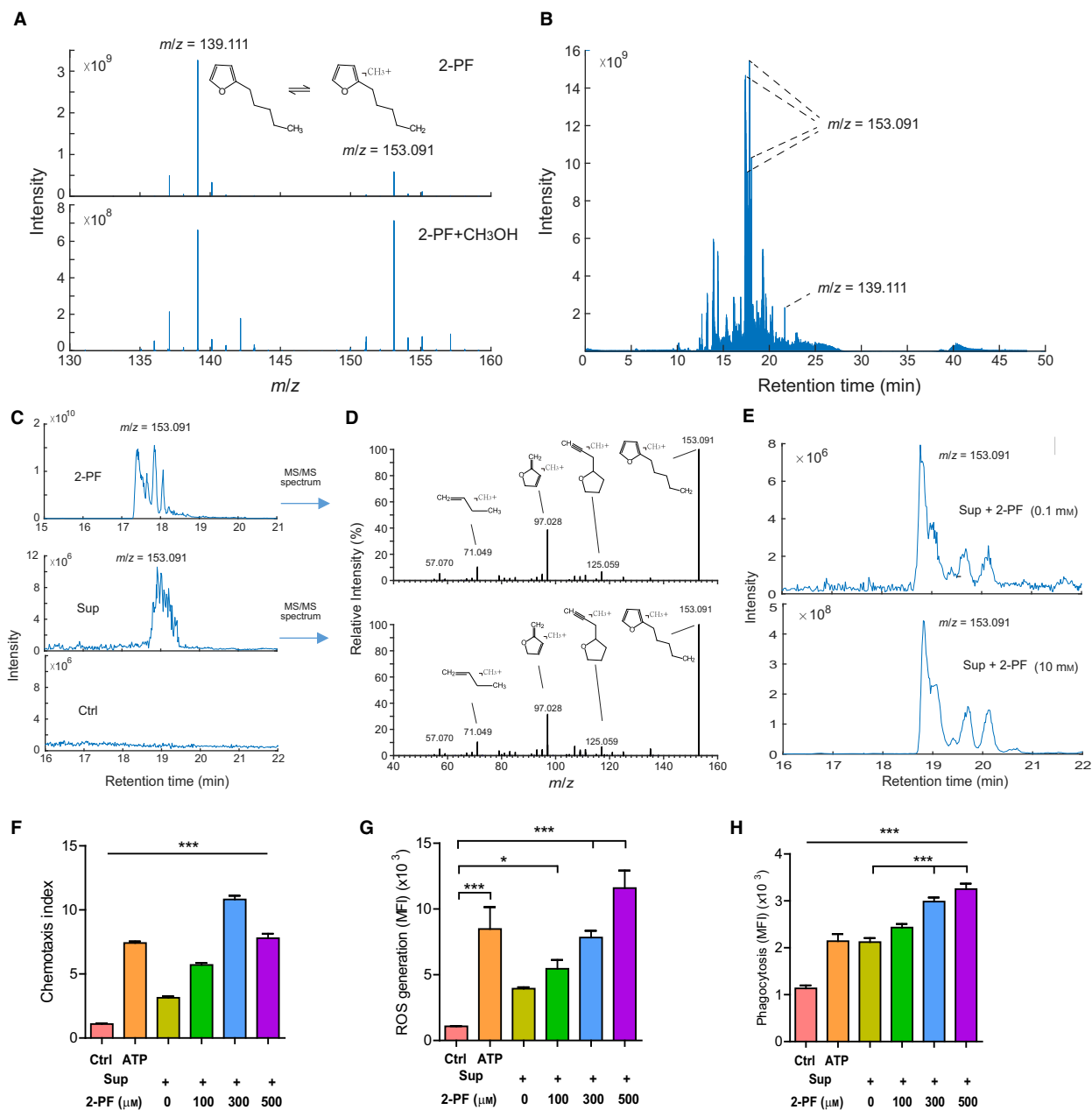


Fig. 4. 2-PF is identified from *S. pneumoniae* culture supernatants. (A) MS spectra of synthetic 2-PF (top) and 2-PF dissolved in methanol (bottom, 2-PF + CH₃OH). The spectra show two precursor ions of 2-PF that correspond to 2-PF ($m/z = 139.111$) and its variant ($m/z = 153.091$), respectively; the latter is in equilibrium with 2-PF. 2-PF is a small organic volatile molecule commonly used for MS analysis after dissolution in CH₃OH. According to the spectra, the variant was more abundant when 2-PF was dissolved in CH₃OH. Because we used 2-PF dissolved in CH₃OH for all LC-MS/MS analyses, we primarily analyzed the variant for identification and quantification of 2-PF in LC-MS/MS datasets. (B) Chromatogram of 2-PF + CH₃OH showing that the variant of 2-PF with $m/z = 153.091$ was most abundant. This observation supports the idea that the 2-PF variant is the most representative ion of 2-PF in 2-PF + CH₃OH. (C) EICs for the precursor ion of 2-PF ($m/z = 153.091$) obtained from LC-MS/MS datasets for synthetic 2-PF, Sup, and control media (Ctrl). (D) MS/MS spectra of 2-PF precursor ions in synthetic 2-PF and Sup. Fragments of the 2-PF precursor ion are shown with their corresponding structures, as predicted by the HMDB [68]. (E) EICs for 2-PF precursor ions in Sup after addition of 0.1 or 10 mM 2-PF. (F–H) Assays for chemotaxis (F), ROS generation (G), and phagocytosis (H), measured after treatment with Sup supplemented with the indicated concentrations of 2-PF (0, 100, 300, and 500 μM) or with control media (Ctrl) and ATP (see text). All bar charts show mean \pm SEM ($n = 5/\text{condition}$, * $P < 0.05$ and *** $P < 0.001$ by one-way ANOVA with Tukey's *post hoc* correction) (F–H).

Table 5. Antibodies used in this study.

Antibodies	Source	Identifier	Working titer
Rabbit anti-Olfr110	Abcam	ab177327	1 : 10 000
Goat anti-Iba1	Abcam	ab5076	1 : 1000
Mouse anti-GFAP	BD Biosciences	556330	1 : 1000
Mouse anti-rhodopsin	Millipore	MABN15	1 : 1000
Rabbit anti-CREB	Cell Signaling Technology	9197	1 : 1000
Rabbit anti-phospho-CREB	Cell Signaling Technology	9198	1 : 1000
Rabbit anti-ERK	Santa Cruz	sc094	1 : 1000
Mouse anti-phospho-ERK	Santa Cruz	sc7383	1 : 1000
Mouse anti-phospho-Akt	Santa Cruz	sc293125	1 : 500
Mouse anti-phospho-JNK	Santa Cruz	sc6254	1 : 500
Mouse anti-phospho-p38	Santa Cruz	sc7973	1 : 1000
Rabbit anti-beta-actin	Cell Signaling Technology	4967	1 : 10 000
Cy3 donkey anti-rabbit	Jackson ImmunoResearch	711-165-152	1 : 1000
Cy3 donkey anti-mouse	Jackson ImmunoResearch	715-165-150	1 : 1000
Alexa Fluor 488 donkey anti-mouse	Jackson ImmunoResearch	715-545-150	1 : 1000
Alexa Fluor 488 donkey anti-goat	Jackson ImmunoResearch	705-545-147	1 : 1000
Anti-rabbit IgG-HRP	Jackson ImmunoResearch	711-035-152	1 : 100 000
Anti-mouse IgG-HRP	Jackson ImmunoResearch	715-035-150	1 : 40 000

this purpose, we introduced the following combinations into the cerebral cortex of CX3CR1^{GFP/+} mice by stereotactic injection [33]: nontargeting siRNA + Mock + siGLO (Ctrl), Olfr110 siRNA + Mock + siGLO (siOlfr110), and Olfr110 siRNA + rescue vector + siGLO (Rescue). Following each injection, we observed brain slices to determine the frequency of transfected MG (yellow) relative to nontransfected MG (green) and transfected nonmicroglia (red) (Fig. 8F). We then microdissected a fluorescence-positive area from the sliced brain and measured expression levels of *Olfr110* using qRT-PCR. Expression of *Olfr110* was significantly reduced ($P < 0.001$) after injection of the ‘siOlfr110’ combination, and this effect was abolished by the injection of the ‘Rescue’ combination (Fig. 8G). By contrast, we did not observe these expression changes after injection of Ctrl, a negative OR control. We did observe similar knockdown and rescue effects on 2-PF-induced phagocytosis in the CX3CR1^{GFP/+} cerebral cortex (Fig. 8H). Taken together, these data suggest that Olfr110 controls representative features of 2-PF-induced microglial activation (cytokine production, ROS generation, chemotaxis, and phagocytosis) *in vitro* and *ex vivo*.

Olfr110-dependent 2-PF-induced microglial activation is regulated by the G_{αs}-cAMP-PKA-ERK and G_{βγ}-PLC-Ca²⁺ pathways

To understand the molecular nature of Olfr110-mediated microglial activation, we performed mRNA-seq analysis of primary MG treated with Sup or 2-PF. From the mRNA-seq data, we identified 1124 and 1438

differentially expressed genes (DEGs) in Sup- and 2-PF-treated MG, respectively, relative to controls (Fig. 9A; Table S1). A significant ($P < 0.01$) fraction of these DEGs (253; 22.5% and 17.6% of 1124 and 1438 DEGs, respectively) were shared between the Sup and 2-PF samples. Among these 253 shared DEGs, 135 and 78 genes exhibited consistent up- and downregulation, respectively, in both Sup- and 2-PF-treated MG, whereas the remaining 40 genes changed in inconsistent directions (Fig. 9B). We next examined cellular processes associated with these overlapping up- and downregulated genes by performing enrichment analysis of gene ontology biological processes (GOBPs). The upregulated genes were mainly associated with processes related to microglial activation (Fig. 9C): cytokine secretion (cytokine production and secretion), chemotaxis (leukocyte migration and chemotaxis), ROS generation (cellular response to ROS and ROS metabolic process), and phagocytosis. These data suggest that both Sup- and 2-PF-induced microglial activation by upregulating genes involved in these processes, whereas the downregulated genes were associated largely with transcriptional regulation (Fig. 9D). We conclude that binding of 2-PF to Olfr110 activates downstream signaling pathways that lead to upregulation of genes involved in microglial activation. To understand downstream signaling, we reconstructed a network model describing interactions among signaling pathways associated with cytokine production, chemotaxis, ROS generation, and phagocytosis (Fig. 9E). The network model revealed that cAMP, mitogen-activated protein kinase (MAPK), phosphoinositide 3-kinases (PI3K), PLC, and Ca²⁺ signaling

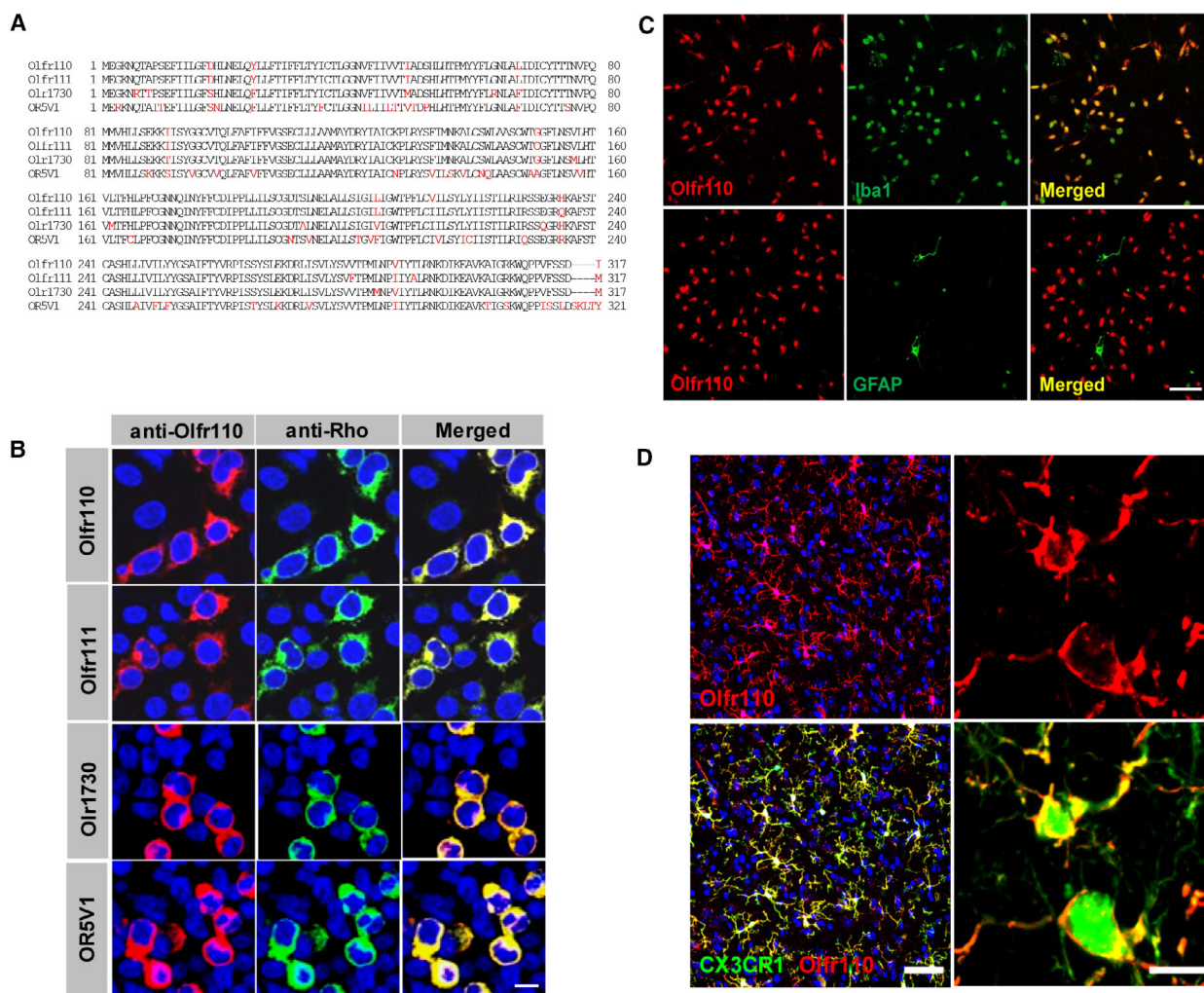


Fig. 5. Characterization of Olfr110 antibody. (A) NCBI BLAST alignment of protein sequences of Olfr110 homologues from mouse, rat, and human by using the Constraint-based Multiple Alignment Tool (COBALT). Amino acid variations in various species are denoted in red. Mouse Olfr110 (accession number: NP_666440, 317 aa); mouse Olfr111 (accession number: NP_001005485, 317 aa); rat Olfr1730 (accession number: NP_001000279, 317 aa); Human OR5V1 (accession number: KP290163, 321 aa). (B) Representative images showing that anti-Olfr110 antibody (anti-Olfr110) captures rhodopsin (Rho)-tagged Olfr110 homologues (Olfr110, Olfr111, Olfr1730, and OR5V1) as efficiently as the Rho antibody (anti-Rho). The Rho sequence tag was added to the N terminus of each Olfr110 homologue, and the resultant constructs were used to transfect to Hana3A cells. Images were obtained after co-staining Hana3A cells expressing each Rho-tagged Olfr110 homologue with anti-Olfr110 (red) and anti-Rho (green). Scale bar: 20 μ m. (C) Representative images showing that expression of Olfr110, measured by anti-Olfr110, correlates with expression of Iba-1 in primary MG (top panels), but not with GFAP in primary AS (bottom panels). Scale bar: 10 μ m. (D) Immunostaining analysis showing expression of Olfr110 (red) in GFP (+)MG (green) in CX3CR1^{GFP/+} cerebral cortex. Left and right panels show low- and high-power images. Scale bar: 50 μ m (left) and 20 μ m (right).

pathways can upregulate genes involved in microglial activation, consistent with previous findings [34].

Hence, we examined the effects of 2-PF on the signaling pathways suggested by the network model. For the cAMP signaling pathway, we measured cAMP levels in primary MG after 2-PF treatment. The cAMP level in MG was increased by 2-PF in a dose-dependent manner, and this effect was blocked by an adenylyl cyclase (AC) inhibitor (Fig. 10A). Olfr110 siRNA decreased this

2-PF-induced cAMP production, and this effect was abolished by the rescue vector (Fig. 10B). To assess the effect on Ca²⁺ signaling, we performed calcium imaging after 2-PF treatment. Intracellular Ca²⁺ levels increased after 2-PF treatment (Fig. 10C; Video S2). To evaluate the MAPK and PI3K signaling pathways, we measured the phosphorylation levels of ERK, p38, c-Jun N-terminal kinase (JNK), and protein kinase B (Akt). We found that the phosphorylation levels were elevated from 2 to

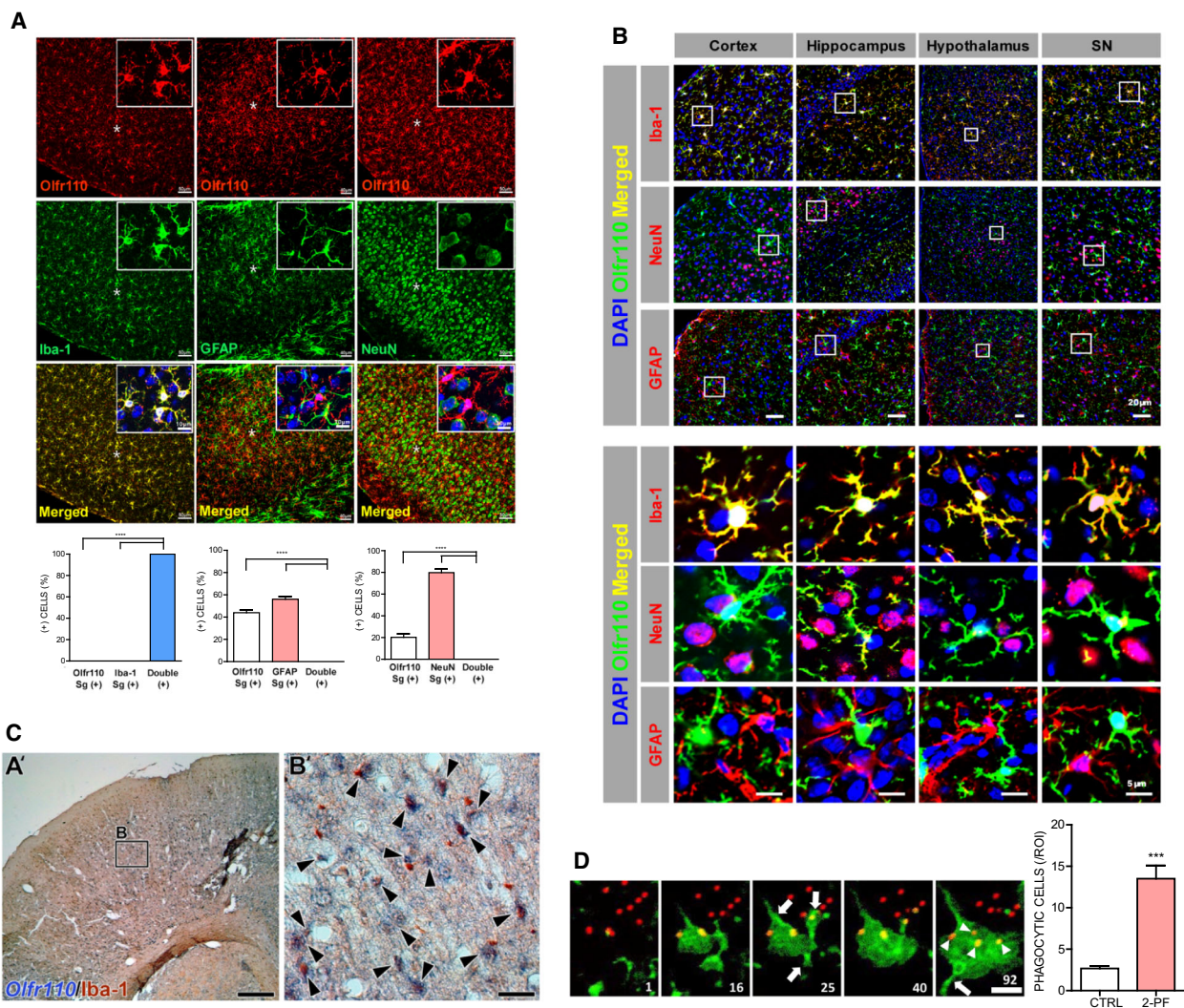


Fig. 6. Olfr110 is expressed in MG. (A) Co-immunostaining analysis showing expression of Olfr110 (red) and Iba-1 (green), a microglial marker, in the cerebral cortex (left panels); expression of Olfr110 and GFAP (green), an astrocyte marker, in the hippocampus (middle panels); and expression of Olfr110 and NeuN (green), a neuronal marker, in the cortex (right panels). DAPI was shown in blue. The area denoted by the asterisk in the low-power images was magnified in the inset. Cells positive to Olfr110 or each marker protein and both proteins were counted from five to seven independent areas with the size of $317.13 \times 317.13 \mu\text{m}^2$ ($n = 3$ mice), and their percentages were shown. Sg (+) and double (+) mean single (+) and double (+) cells, respectively. Results are the means \pm SEM of five to seven independent areas ($n = 15\text{--}21$, $P < 0.0001$ by one-way ANOVA with Tukey's *post hoc* correction). Scale bar: 40 or 50 μm for low-power images and 10 μm for high-power images. (B) Representative images showing co-immunohistochemical staining of Olfr110 (green) with Iba-1 (red), GFAP (red), or NeuN (red) in various brain regions: cortex, hippocampus, hypothalamus, and SN. The bottom panel shows a higher-magnification image of the square in the top panel. Scale bars: 20 μm (top panel), 5 μm (bottom panel). (C) Expression pattern of *Olfr110* mRNA and protein localization of Iba-1 in C57BL/6J mouse adult brain at 9 weeks. Sequential analysis followed by *in situ* hybridization (blue, NBT/BCIP staining) for *Olfr110* and IHC (brown, DAB staining) for Iba-1. (A') Low-magnification image for *Olfr110* expression and Iba-1 protein. (B') High-magnification image of *Olfr110* transcripts and Iba-1 labeling of MG. Black box in A' indicates a high-magnification region. Black arrowheads in B' indicate colocalization of *Olfr110* and Iba1. Scale bars: (A') 250 μm ; (B') 25 μm . (D) Representative time-lapse confocal microscopy images showing volume (green) and protruding processes (arrow) of MG measured in cerebral cortex slices at five different time points (1, 16, 25, 40, and 92 min) after treatment with Ctrl or 2-PF. Beads that were phagocytosed (arrowheads) or not phagocytosed (red) are shown at each time point during the phagocytosis assay. MG with phagocytosed beads were counted in six different locations in each of three independent mice after treatment with Ctrl or 2-PF. Counts are displayed in the bar plot. Scale bar: 10 μm . Bar charts show mean \pm SEM ($n = 12\text{--}16$, $P < 0.001$ by one-way ANOVA with Tukey's *post hoc* correction).

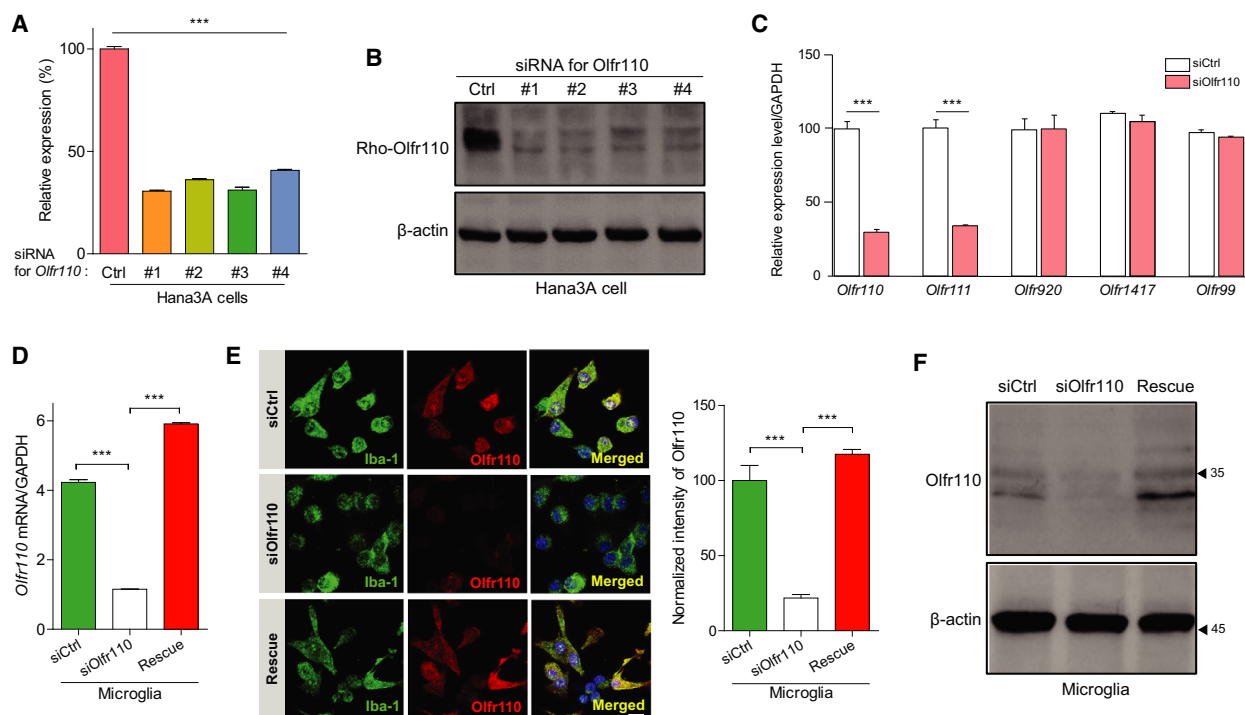


Fig. 7. Development of specific siRNA and rescue vector for Olfr110. (A, B) Relative mRNA (A) and protein (B) expression levels of Olfr110 measured in Hana3A cells transfected with Olfr110 siRNAs #1 to #4, as determined by qRT-PCR ($n = 3$, $P < 0.001$ by one-way ANOVA with Student's t -test) and western blot analyses, respectively. In western blot analysis, we detected rho-tagged Olfr110 by anti-rho antibody. GAPDH and β -actin were used as internal and loading controls for qRT-PCR and western blot analyses, respectively. Data are means \pm SEM (C) Specificity of Olfr110 siRNA #3 on *Olfr110* and *Olfr111*. Three major ORs (*Olfr920*, *Olfr1417*, and *Olfr99*) in primary MG were used as negative controls ($n = 3$, $***P < 0.001$ by one-way ANOVA with Student's t -test). (D) Relative mRNA expression levels of Olfr110 measured in primary MG transfected with nontargeting siRNA + Mock (siCtrl), Olfr110 siRNA + Mock (siOlfr110), or Olfr110 siRNA + rescue vector (Rescue) after 2-PF treatment ($n = 3$, $***P < 0.001$ by two-way ANOVA with Tukey's *post hoc* correction). (E) Representative images showing expression of Olfr110 in primary MG under siCtrl, siOlfr110, and Rescue conditions. Olfr110 (red) was costained with Iba-1 (green), a microglial marker, under each condition. Fluorescence intensity of Olfr110 in the image was quantified in three different mice ($n = 3$, $P < 0.001$ by two-way ANOVA with Tukey's *post hoc* correction). Scale bar: 20 μ m. (F) Western blot with anti-Olfr110 antibody showing the level of Olfr110 using the same conditions shown (E).

20 min after 2-PF treatment (Fig. 10D). Next, we used specific inhibitors to examine the relative contributions of these signaling pathways to microglial activation. After pretreatment with AC (SQ22536), PKA (H-89), ERK (PD98059), or PLC inhibitor (U73122), we measured protein levels of TNF- α and IL6 following 2-PF treatment. SQ22536 or H-89 dramatically decreased the levels of both cytokines, whereas PD98059 and U73122 caused weaker reductions (Fig. 10E). U73122, but not other inhibitors, completely ($P < 0.001$) inhibited ROS generation (Fig. 10F). ROS generation was similarly inhibited by gallein, an inhibitor of $G_{\beta\gamma}$, which can activate PLC [35,36]. All inhibitors significantly ($P < 0.05$) reduced phagocytic activity (Fig. 10G) and almost completely ($P < 0.001$) abolished chemotactic activity (Fig. 10H). In addition, phosphorylation levels of cAMP response element-binding protein (CREB) and ERK were dramatically decreased by SQ22536 and

PD98059 (Fig. 10I). Based on these data, we propose the following model: both the $G_{\alpha s}$ -cAMP-PKA-ERK and $G_{\beta\gamma}$ -PLC-Ca $^{2+}$ pathways regulate cytokine production, chemotaxis, and phagocytosis, whereas the $G_{\beta\gamma}$ -PLC-Ca $^{2+}$ pathway is predominantly responsible for ROS generation (Fig. 11).

Discussion

In this study, we demonstrated that Olfr110 and Olfr111, which are primarily expressed in MG, recognize a pathogenic metabolite, 2-PF, secreted by *S. pneumoniae*. The 2-PF-Olfr110 interaction leads to microglial activation, which in turn induces chemotaxis, cytokine production, phagocytosis through the $G_{\alpha s}$ -cAMP-PKA-ERK and $G_{\beta\gamma}$ -PLC-Ca $^{2+}$ pathways, as well as ROS generation through the latter pathway. Elucidating the molecular basis of this interaction is

important because pathogen-derived small metabolites can serve as biomarkers for pathogen infections, and because it provides novel insights into functions associated with neuroinflammation. In addition, greater knowledge of these interactions could provide fundamental insight into the physiological and pathological roles of ectopically expressed ORs.

Olfr110 mRNA is expressed in cerebral cortex of wild-type mice and the APP/PS1 transgenic model of AD [25], as well as in the hippocampus of a mouse model of gestational ethanol exposure [37]. In this study, we found that mouse *Olfr110* and *Olfr111* (human ortholog, OR5V1; rat one, *Olr1730*; Fig. 5A,B) were predominantly expressed in MG in four different brain areas (cortex, hippocampus, hypothalamus, and SN), but only residually in other cell types in these areas (Fig. 6A,B). CX3CR1-GFP transgenic mice, which express GFP in MG, revealed that *Olfr110* expression largely overlapped with GFP-positive cells, as indicated by the large proportion of yellow signals in Fig. 5D. These reproducible observations were confirmed by sequential analysis in which *in situ* hybridization for *Olfr110* transcript was followed by IHC for Iba-1 (Fig. 6C). Moreover, Zhang *et al.* [31] showed that *Olfr110* and *Olfr111* are more highly expressed in MG than in other brain cell types (Table 1), and that among the ORs, *Olfr110* and *Olfr111* were predominantly expressed in MG. Also, Schaum *et al.* [38] used single-cell RNA-sequencing to show that *Olfr110* and *Olfr111* genes are predominantly expressed in MG and that they are the most highly expressed ORs in MG (<https://tabula-muris.ds.czbiohub.org>). Taken together, all these data suggest that *Olfr110* and *Olfr111* are mainly expressed in MG, but only residually in astrocyte and neuron in the brain.

Our *in vitro* and *ex vivo* experiments demonstrated that the 2-PF–*Olfr110*/*Olfr111* induced microglial activation. However, for this reaction to occur under physiological conditions, 2-PF must be produced and transferred to the brain in the range of ten to hundreds of micromolar. The physiological concentration of 2-PF in the vicinity of its receptor is a critical issue. In this study, we estimated the EC_{50} value of 2-PF for *Olfr110* by treating *Olfr110*-transfected Hana3A cells with 2-PF *in vitro*. However, the actual EC_{50} value of 2-PF for *Olfr110* and *Olfr111* may be low *in vivo*. For example, accessory proteins that promote effective targeting of ORs to the plasma membrane *in vivo* can lower EC_{50} values [39] such that a small amount of 2-PF can stimulate *Olfr110* and *Olfr111*. Moreover, 2-PF-derived metabolic derivatives capable of stimulating *Olfr110* at low EC_{50} values may be generated under physiological conditions in the brain, as previously described in nasal mucus [40]. Furthermore, 2-PF may be present in complex with

an odorant-binding protein or lipocalin *in vivo* [41,42], which can increase its solubility and thereby enable even trace amounts of 2-PF to bind *Olfr110*/*Olfr111*.

Many ORs have been identified in nonchemosensory tissues and cells of the body [17,18], and their functions have been elucidated individually *in vivo* [16,43–45]. Although few studies have focused on OR expression in the brain [23], the Ferrer group has consistently identified dysregulated ORs in neurodegenerative and neuropsychiatric diseases of human and murine [24,25,27,46]. In an AD-like APP/PS1 animal model, *Olfr110* expression was elevated at 3, 6, and 12 months of age, indicating that augmented expression of ORs in aged mice is not due to neuronal loss, but instead to a regulated pathological response [25]. Consistent with this, another study identified ORs in the cortex and hippocampus of wild-type and 5× FAD mice and showed that they were localized near amyloid plaques with age [26]. In this study, we also identified *Olfr110* and *Olfr111* from MG and showed that they were predominantly expressed in MG in various regions throughout the brain. In addition, we identified 2-PF secreted from a pathogen as a ligand for *Olfr110* and *Olfr111*, and demonstrated that the 2-PF–*Olfr110*/*111* interaction induced MG activation accompanied by cytokine production, chemotaxis, phagocytosis, and ROS generation.

In summary, *Olfr110* and *Olfr111* expressed in MG recognize invading pathogens by detecting secreted 2-PF and then eliminate the pathogens through microglial activities such as chemotaxis and phagocytosis; this is the beneficial effect of OR expression in MG. However, excessive levels of this metabolite can cause inflammation in the brain, accompanied by microglial hyperactivation and pro-inflammatory cytokine secretion, ultimately leading to pathological effects such as chronic neuroinflammation. In previous studies [25,26], the increasing expression of *Olfr110* with age and the expression of *Olfr110* near the amyloid plaque in animal models of neurodegenerative diseases were considered to represent evidence of chronic neuroinflammation due to hyperactivated MG overexpressing *Olfr110*. Further studies are required to address this question in animal models. From the standpoint of recent proposals for targeting ORs with therapeutic drugs [22,47], *Olfr110* represents a target, and 2-PF or its derivatives a candidate drug, for the treatment of neuroinflammation-related brain diseases.

Metabolites such as propane, butane, and 3-methylbutanal derived from *Staphylococcus aureus* serve as breath biomarkers to diagnose ventilation-associated pneumonia [48]. Interestingly, 2-PF derived from *S. pneumoniae* detected in the exhalations of patients with cystic fibrosis could serve as a diagnostic

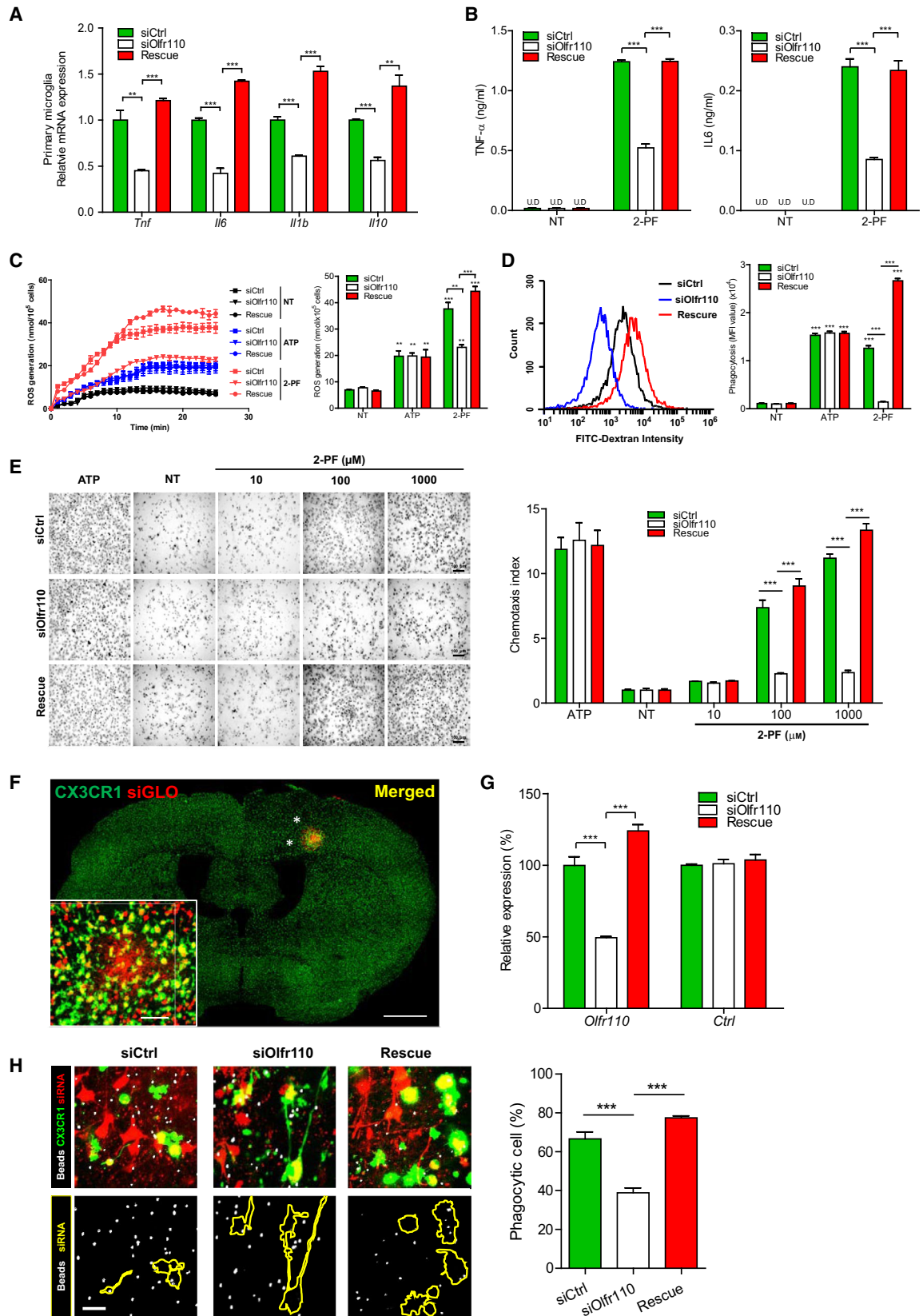


Fig. 8. Olfr110 controls microglial activation induced by 2-PF. (A) Levels of mRNAs encoding inflammatory cytokines (*Tnf*, *Il6*, *Il1b*, and *Il10*) after 2-PF treatment in primary MG transfected with nontargeting siRNA + Mock (siCtrl), siRNA against Olfr110 + Mock (siOlfr110), and siRNA against Olfr110 + rescue vector (Rescue) ($n = 3/\text{condition}$, $**P < 0.01$ and $***P < 0.001$ by two-way ANOVA with Tukey's *post hoc* correction). siRNA + Mock or rescue vector transfection was done at 24 h earlier than 2-PF treatment. (B) Protein levels of TNF- α and IL6 in culture supernatants from primary MG after siRNA transfection followed by 2-PF treatment, as described in (A) ($n = 3/\text{condition}$, $P < 0.001$ by two-way ANOVA with Tukey's *post hoc* correction). U.D. means undetermined. (C) Accumulated amounts of O_2^- generated in primary MG after siRNA transfection followed by 2-PF treatment (red). Measurements were performed at 1-min interval for 25 min. Total amount at 25 min is displayed in the bar plot ($n = 3/\text{condition}$, $**P < 0.01$ and $***P < 0.001$ by two-way ANOVA with Tukey's *post hoc* correction). Experiments were repeated after treatment with control solvent (NT; black) or positive control (ATP; blue). (D) Distribution of FITC-dextran intensities in primary MG after siRNA transfection followed by treatment of 2-PF, NT, or ATP as described in (C), as determined by FACS analysis. Phagocytosis index shows quantified MFIs ($n = 5/\text{condition}$, $P < 0.001$ by two-way ANOVA with Tukey's *post hoc* correction). (E) Representative images showing migrated primary MG measured under three different concentrations (10, 100, and 1000 μM) of 2-PF. Chemotaxis index represents quantified counts of migrated MG ($n = 3/\text{condition}$, $P < 0.001$ by two-way ANOVA with Tukey's *post hoc* correction). Scale bar: 100 μm . (F) Representative brain slice image showing transfected MG (yellow), nonmicroglia (red, siGLO), and nontransfected MG (green) in CX3CR1^{GFP/+} cerebral cortex after the stereotactic injection. The area denoted by the asterisk in the whole brain was magnified in the inset. Scale bar: 1 mm. (G) mRNA expression levels of *Olfr110* or Ctrl, a negative OR control, measured in the microdissected asterisked area (F) by qRT-PCR ($n = 3/\text{condition}$, $P < 0.001$ by two-way ANOVA with Tukey's *post hoc* correction) after injection of nontargeting siRNA + Mock + siGLO (Ctrl); Olfr110 siRNA + Mock + siGLO (siOlfr110); or Olfr110 siRNA + rescue vector + siGLO (Rescue). (H) Representative images showing distributions of beads in the three types of cells (top panels; see legend in F) in CX3CR1^{GFP/+} cerebral cortex under siCtrl, siOlfr110, and Rescue conditions. Bottom panel shows transfected MG (yellow lines) with beads (white dots). Scale bar: 20 μm . MG enclosing beads, representing engulfing MG, were counted in six different locations in three independent mice under each of the three conditions. Counts are displayed in the bar plot ($n = 3/\text{condition}$, $P < 0.001$ by two-way ANOVA with Tukey's *post hoc* correction). All bar charts show mean \pm SEM.

biomarker for cystic fibrosis [49]. Beyond its utility as a diagnostic biomarker, in this study we identified 2-PF from *S. pneumoniae* culture supernatants (Fig. 4A-E) and demonstrated its functional role in microglial activation. Specifically, we showed that 2-PF interacts with Olfr110, a GPCR predominantly expressed in MG. This interaction induces microglial activation, suggesting a unique small metabolite-mediated pathogen–brain axis associated with neuroinflammation. Conventional PRRs involved in microglial activation are receptors for pathogen-derived macromolecules, including cell wall components, peptidoglycan, lipoteichoic acid, and flagellin [10,50]. Our findings provide an alternative strategy for pathogen recognition by MG that involves small metabolite–OR interactions.

Materials and methods

Bacterial culture

Encapsulated serotype 2 *S. pneumoniae* strain D39 [8] was cultured on THY agar plates: sterilized Todd–Hewitt media containing 30 $\text{g}\cdot\text{L}^{-1}$ of Todd–Hewitt Broth (#249240; BD Biosciences, Franklin Lakes, NJ, USA), 0.5% yeast extract (#288620; BD Biosciences), and 1.5% agar. Subsequently, the bacteria were transferred into THY broth (i.e., the same medium lacking agar) and cultured in an incubator at 37 °C for 24–48 h until OD₅₅₀ reached 0.3, corresponding to a concentration of 10⁸ colony-forming units per mL. The culture supernatants (Sup) were separated by centrifugation at 4000 g at 4 °C for 10 min and then used in experiments. To

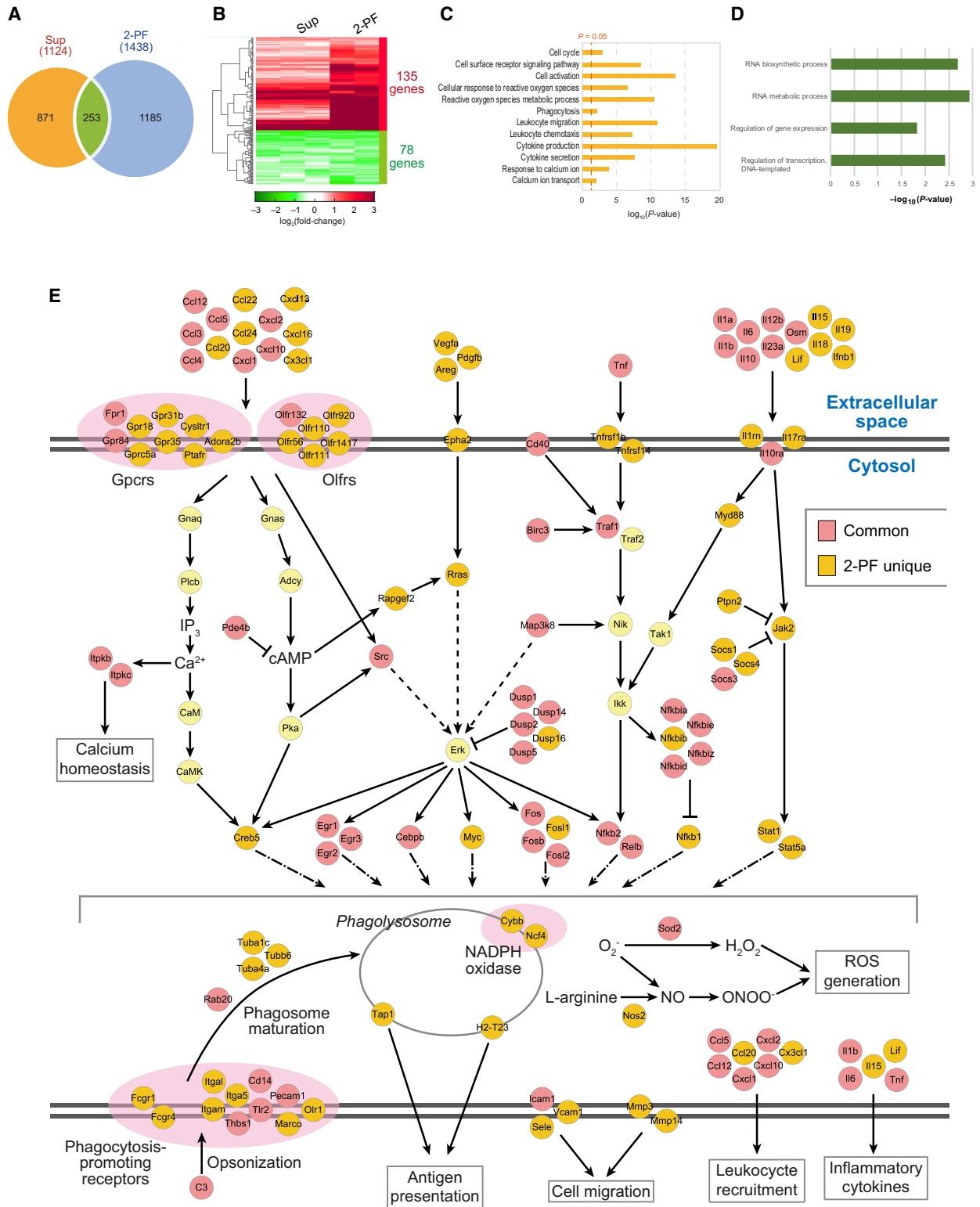
isolate the fraction containing small metabolites, Sup was filtered through an Ultracel YM-3 membrane (3 kDa pore; Millipore Corporation, Bedford, MA, USA).

Animals

Eight- to 10-week-old C57/BL6J or heterozygous CX3CR1^{+GFP} mice [51] were used for *ex vivo* phagocytosis, *in situ* hybridization, and IHC assays. CX3CR1^{+GFP} mice were generated by cross-breeding C57/BL6J with CX3CR1^{GFP/GFP}. All mice were housed at room temperature under a 12-h light/dark cycle with access to sterile food and water *ad libitum*. All animal procedures were conducted according to the guidelines on the care and use of laboratory animals, as approved by the Daegu Gyeongbuk Institute of Science and Technology's Institutional Animal Care and Use Committee (DGIST-IACUC 19052304-00).

Culture of primary microglia and astrocytes

Primary MG or AS were obtained from the brain cortex of E18.5 mouse (C57BL6/N; KOATECH, Pyeongtaek, Korea) embryos and cultured as previously described with slight modifications (DGIST-IACUC-19041202-02) [52,53]. Briefly, after dissection of the embryonic cortex, collected brains were stored in ice-cold Hanks' balanced salt solution (#14170-112; Thermo Fisher Scientific, Waltham, MA, USA) and digested with 0.25% trypsin (#15090-046; Thermo Fisher Scientific) for 20 min at 37 °C. Cells were suspended in plating medium supplemented with minimum essential medium (#11095-080; Thermo Fisher Scientific),



10% FBS (#SH30919.03; Hyclone, S. Logan, UT, USA), 2 mM L-glutamine (#25030-081; Thermo Fisher Scientific), 0.04% glucose (#G7021; Sigma-Aldrich, St Louis, MO,

USA), and 1% penicillin/streptomycin (#15140-122; Thermo Fisher Scientific), and the suspension was filtered through a 40- μm strainer (#352340; Thermo Fisher

Fig. 9. Signaling pathways underlying Olfr110-dependent 2-PF-induced microglial activation. (A) Relationship between DEGs from comparisons of Sup-treated vs. control MG (Sup) and 2-PF-treated vs. control MG (2-PF). Numbers of DEGs from the corresponding comparisons are indicated in parentheses. (B) Heat map showing \log_2 -fold changes of up- (red) and downregulated (green) genes in the two comparisons. Hierarchical clustering to generate the dendrogram was performed based on \log_2 -fold changes in individual samples. Numbers of up- and downregulated genes are indicated. Color bar shows the gradient of \log_2 -fold changes. (C) GOBPs enriched among upregulated genes in Sup and 2-PF-treated MG. Enrichment P -values for GOBPs are shown as $-\log_{10}(P\text{-value})$. Dotted line indicates the cutoff for enrichment P -value ($P = 0.05$). (D) GOBPs enriched among downregulated genes in Sup and 2-PF-treated MG. Enrichment P -values for GOBPs are shown as $-\log_{10}(P\text{-value})$. Dotted line indicates the cutoff of the enrichment P -value ($P = 0.05$). (E) Network model describing signaling pathways associated with processes related to microglial activation (chemotaxis, ROS generation, cytokine production, and phagocytosis). Magenta nodes represent genes upregulated by both Sup and 2-PF, whereas orange nodes represent genes upregulated only by 2-PF. Arrows and suppression symbols denote activation and inhibition, respectively, in signaling cascades. Dotted arrows indicate indirect activation (i.e., through intermediate molecules) between nodes connected by the arrows. Plasma membrane is indicated by two thick lines. Nodes are arranged based on information in the Kyoto Encyclopedia of Genes and Genomes pathway database.

Scientific) by a process of trituration; the product of this manipulation was retained as the FT fraction. Mixed glial cells were plated at a density of 1.2×10^7 cells in T75 flasks precoated with poly-D-lysine (#P7280; Sigma-Aldrich). After 2 h, the plating medium was replaced with a mixed glial cell growth medium: Dulbecco's modified eagle medium (DMEM; #SH30243.01; Hyclone) supplemented with 10% FBS and 1% penicillin/streptomycin. The resultant mixed glial cells were incubated with growth medium, which was replaced every 3 days for 2 weeks. For isolation of primary MG from mixed glial cells, the cells were shaken for 2 h at 150 r.p.m. at 37 °C to allow MG to detach from the astrocyte monolayer within the flasks. The supernatant containing the floating MG was collected and centrifuged at 1300 g for 5 min at room temperature. The resulting cell pellet was resuspended in MG culture medium. After the MG-containing supernatant was removed, the flasks were shaken at 160 r.p.m. for 1 day in a shaking incubator to completely remove primary MG. AS were then detached by digestion with 0.25% trypsin, collected, replated in a T75 flask, and incubated for 4 days. The purity of primary MG or AS was assessed by qRT-PCR and immunocytochemistry to detect marker genes and proteins (Iba-1 and Gfap), respectively.

RNA extraction and quantitative real-time PCR analysis (qRT-PCR)

Total RNA was extracted from primary MG, primary AS, or Hana3A cell using a MagNA Lyser (Roche Molecular Diagnostics, Pleasanton, CA, USA) with TRIzol reagent (#15596-026; Invitrogen, Carlsbad, CA, USA). Contaminating DNA was depleted with Riboclear *plus* (#313-150; GeneAll, Seoul, Korea). Two micrograms of RNA were reverse-transcribed into cDNA using the PrimeScript™ First-Strand cDNA Synthesis kit (#6110; Takara Bio Inc., Kusatsu, Japan). Using the resultant cDNA, qRT-PCR was performed with LightCycler® 480 SYBR Green I Master on a LightCycler® 96 Real-Time PCR system (Roche Molecular Diagnostics). The relative

expression levels of target mRNAs were calculated using the $2^{-\Delta\Delta C_t}$ method [54]. The primers used are summarized in Table 6 [55,56].

Cytokine ELISA assay

The levels of TNF- α , IL6, and IL1b secreted from primary MG were determined by ELISA 24 h after treatment with Sup or 2-PF. The ELISA kits were purchased from BD Biosciences (#DY410 for TNF- α ; #DY406 for IL6; #DY401 for IL1b).

Measurement of superoxide (O_2^-) levels

Superoxide (O_2^-) levels were measured by cytochrome c reduction assay on a VersaMax microplate reader (Molecular Devices, San Jose, CA, USA) as previously described [57] with modifications. Primary MG (1.0×10^5 cells/well in 96-well plates) were stimulated with 2-PF, Sup, or 10 μ M ATP in the presence of cytochrome c (50 μ M; #C2037; Sigma-Aldrich) and cytochalasin B (5 μ M; #C66762; Sigma-Aldrich). The ROS level was calculated based on the change in light absorption at 550 nm over 25 min, measured at 1-min intervals.

Chemotaxis

Chemotaxis was measured using a multi-well Boyden chamber as previously described [58]. Briefly, polycarbonate filters (8 μ m pore; #101-8; NeuroProbe, Gaithersburg, MD, USA) were coated with 10 mg·mL⁻¹ fibronectin (Sigma-Aldrich) in PBS for 2 h. A dry-coated filter was installed in a Boyden chamber in which the bottom wells were filled with serum-free DMEM containing 2-PF or Sup at the aforementioned concentrations. MG or Hana3A cells transfected with the OR construct were suspended in serum-free DMEM, placed in the top wells, and incubated at 37 °C for 4 (MG) or 8 h (Hana3A). Cells that migrated to the bottom side were fixed with 4% PFA and stained with hematoxylin for 10 min. Migrated cells were counted under a light microscope in five randomly chosen high-power fields (200 \times) using a scored eyepiece. Chemotaxis index

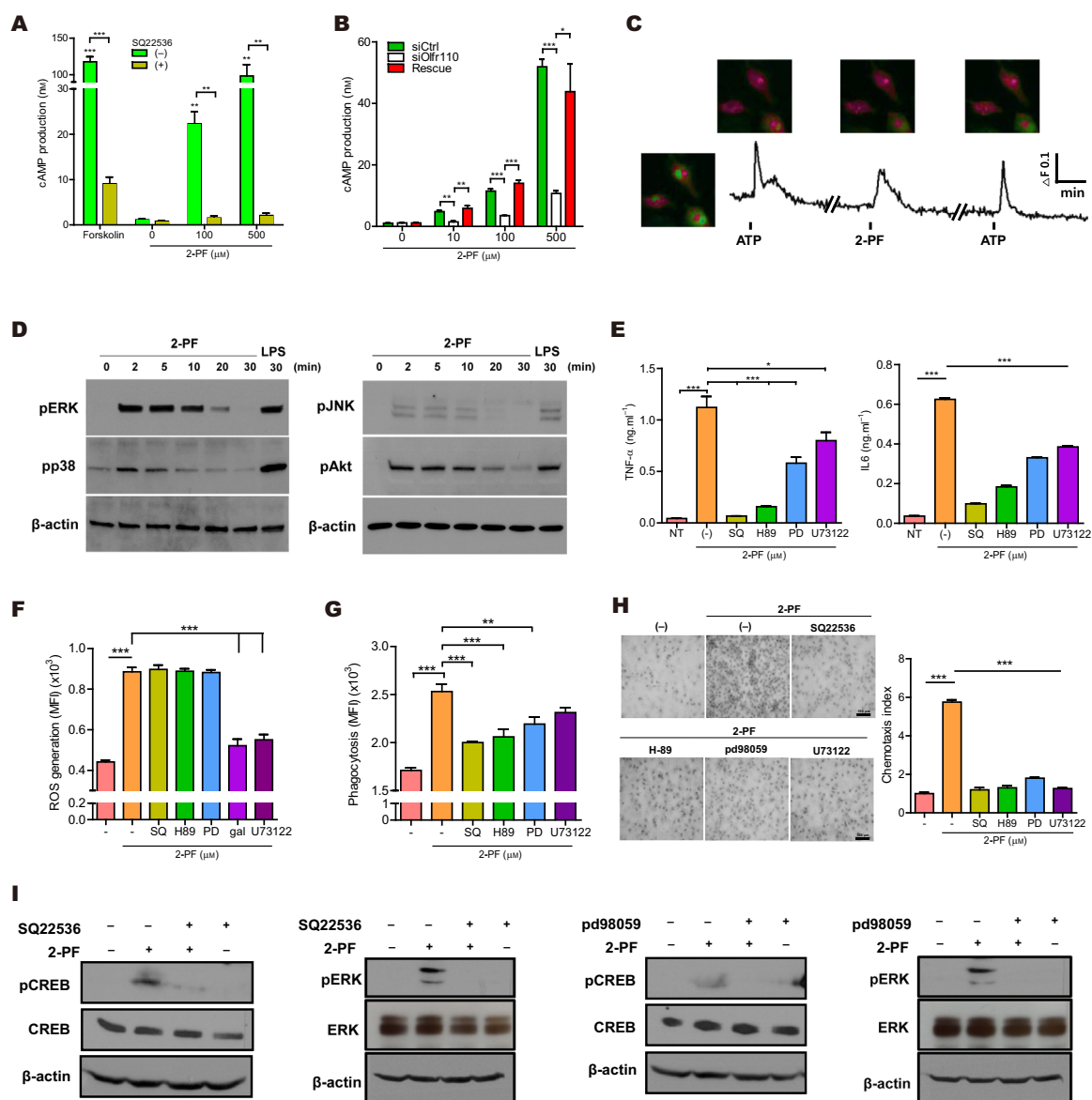
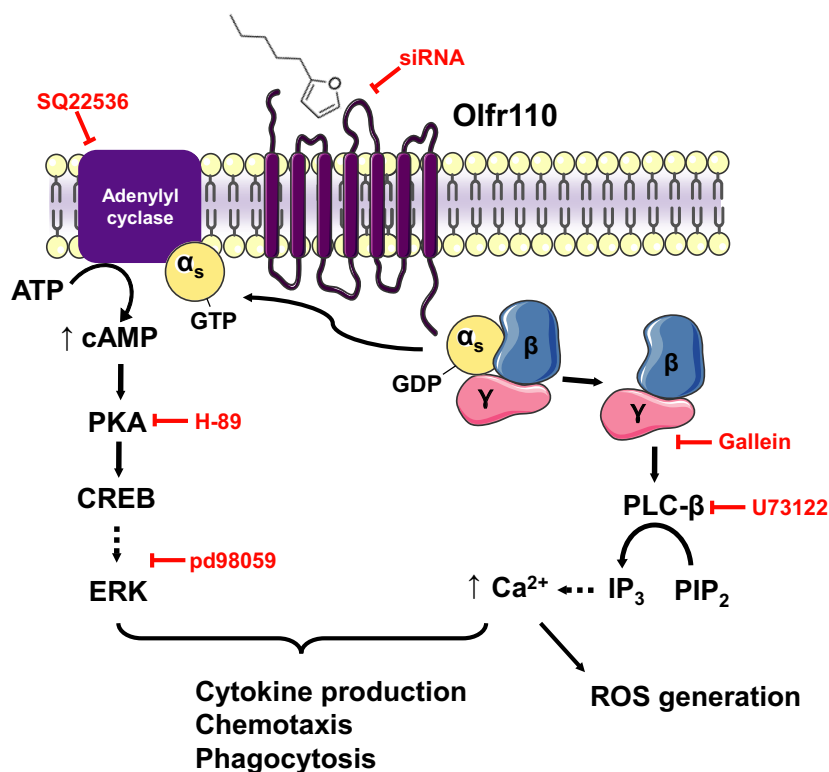


Fig. 10. Olfr110-dependent 2-PF-induced microglial activation is regulated by $G_{\alpha s}$ -cAMP-PKA-ERK and $G_{\beta\gamma}$ -PLC- Ca^{2+} pathways. (A) cAMP production measured in primary MG after treatment of different concentrations (0, 100, and 500 μ M) of 2-PF with or without pre-incubation of SQ22536 (AC inhibitor). Bar charts show mean \pm SEM ($n = 3$ /condition, $**P < 0.01$ and $***P < 0.001$ by two-way ANOVA with Tukey's *post hoc* correction). Forskolin, an AC activator, was used as a positive control. (B) cAMP production measured in primary MG after treatment with the same concentrations of 2-PF under siCtrl, siOlfr110, and Rescue conditions (see legend in Fig. 8A). Bar charts show mean \pm SEM ($n = 3$ /condition, $*P < 0.05$, $**P < 0.01$, and $***P < 0.001$ by two-way ANOVA with Tukey's *post hoc* correction). (C) Representative images showing increased amounts of intracellular calcium in primary MG after treatment of 100 μ M 2-PF. Colors represent high (red) and low (green, baseline) concentrations of calcium, as determined by fura-2AM calcium imaging. ATP was used as a positive control before and after treatment with 2-PF. Y-axis shows fluorescence ratio (F340/F380 nm), and x-axis shows time (see scale bar). (D) Levels of phosphorylated ERK (pERK), p38 (pp38), JNK (pJNK), and Akt (pAkt) were measured in primary MG by western blot analysis at 0, 2, 5, 10, 20, and 30 min after treatment of 2-PF. LPS was used as a positive control and β -actin as a loading control. (E) Levels of TNF- α and IL6 secreted from primary MG after treatment with 2-PF with or without pre-incubation with AC (SQ: SQ22536), PKA (H89), ERK (PD: pd98059), or phospholipase C (U73122) inhibitor. ($n = 3$ /condition, $*P < 0.05$ and $***P < 0.001$ by one-way ANOVA with Tukey's *post hoc* correction). (F–H) ROS generation (F), phagocytosis (G), and chemotaxis activity (H) measured as described in (E). For details, see the legend of Fig. 1D–F. Representative images of migrated primary MG are also shown in (H). Bar charts show means \pm SEM ($n = 5$, $**P < 0.01$ and $***P < 0.001$ by one-way ANOVA with Tukey's *post hoc* correction). Scale bar: 100 μ m. (I) Amounts of ERK, phosphor-ERK (pERK), CREB, and phosphor-CREB (pCREB) measured in primary MG by western blot analysis after treatment with 2-PF and pre-incubation with SQ22536 or PD98059.

Fig. 11. Molecular mechanism for Olfr110-dependent 2-PF-induced microglial activation. Binding of 2-PF to Olfr110 promotes the conversion of G proteins from their guanosine diphosphate bound forms to their active guanosine triphosphate-bound forms ($G_{\alpha s}$). Activated $G_{\alpha s}$ then activates AC to produce cAMP, which in turn activates PKA, CREB, and ERK. On the other hand, dissociated $G_{\beta\gamma}$ activates PLC- β and then IP_3 , which in turn increases the level of intracellular calcium. The activated $G_{\alpha s}$ -cAMP-PKA-ERK and $G_{\beta\gamma}$ -PLC- Ca^{2+} pathways regulate cytokine production, chemotaxis, and phagocytosis, whereas the $G_{\beta\gamma}$ -PLC- Ca^{2+} pathway is predominantly responsible for the regulation of ROS generation. Inhibitors or siRNAs used to infer the contribution of individual signaling pathways are indicated in red.



was defined as the migrated cell number normalized against that in the untreated group.

Phagocytosis assay

Primary MG were seeded in 24-well plates (5×10^5 cells/well) and incubated for 24 h. Cells were preincubated with 2-PF or Sup for 30 min, incubated with fluorescein isothiocyanate (FITC)-dextran ($1 \text{ mg}\cdot\text{mL}^{-1}$, $20 \text{ mg}\cdot\text{mL}^{-1}$ in PBS as stock; #FD70S; Sigma-Aldrich) in serum-free DMEM at 37°C for 30 min, and washed with PBS at 4°C . Cells were detached by digestion with 0.25% trypsin (#15090-046; Thermo Fisher Scientific) in PBS, and detached cells were analyzed on a FACS Accuri™ C6 flow cytometer (BD Biosciences). Mean fluorescence intensity (MFI) was calculated by integrating the fluorescence histograms for cells under each condition using the BD Accuri™ C6 software. Phagocytosis index was defined as MFI in the sample, normalized against MFI in the untreated group.

Measurement of ROS levels

Reactive oxygen species levels were measured using 2',7'-dichlorodihydrofluorescein diacetate (DCF-DA, #D6883; Sigma-Aldrich) as previously described [59] with minor modifications. Briefly, primary MG were seeded in 24-well plates (5.0×10^5 cells/well) for 24 h and then treated with $10 \mu\text{M}$ DCF-DA at 37°C for 30 min in the presence or

absence of 2-PF (or Sup). The cells in each well were analyzed by a FACS Accuri™ C6 flow cytometer, and MFI was determined as described above.

Table 6. Primer pairs used in this study.

Primer		Sequence
<i>Olfr110</i>	F	GTGTTGCACACGGTTTTGAC
	R	AAGGATGACGCACAGGAAAG
<i>Olfr111</i>	F	ACACCGTCTTGACCTTCCAC
	R	AGGAAAGGATGATGCACAGG
<i>Olfr920</i>	F	TGATGGGGTTTTCTGGTGCT
	R	TGACATAGGTGCTGGTGACG
<i>Olfr1417</i>	F	TCCTGCAGTATGGATGTGGA
	R	CACCACCTTCCTCAAAGCAT
<i>Olfr99</i>	F	TGTGGACTGGAGATGGATCA
	R	TGAGTAGCGCAGTGGATGAC
<i>Tnf</i>	F	ACTGAACTTCGGGGTGATCG
	R	GTTTGCTACGACGTGGGCTA
<i>Il6</i>	F	AGACAAAGCCAGAGTCCCTCA
	R	GTTTGCTACGACGTGGGCTA
<i>Il1b</i>	F	AATGCCACCTTTTGACAGTGAT
	R	CCTGCCTGAAGCTCTTGTTG
<i>Il10</i>	F	ACTTGGGTTGCCAAGCCTTAT
	R	AGGGTCTTCAGCTTCTCACC
<i>Il13</i>	F	CAACCCCGAGCTAGTTGTCA
	R	CCTTGCTGTGAGGACGTTTG
<i>GAPDH</i>	F	GGAGAGTGTTCCTCGTCCC
	R	ATGAAGGGGTCTTGTATGGC

Odorant receptor (OR) construct cloning and surface localization

Full-length ORs from mouse, rat, or human genomic DNA were amplified using the appropriate primers. The resultant cDNAs were digested with restriction enzymes, and the products were ligated to generate OR constructs with the restriction sites in mammalian expressing vector PME18S containing N-terminal Lucy, FLAG, and Rho tags, as previously described [60,61]. All OR constructs were confirmed by sequencing. These constructs were then transfected into Hana3A cells with receptor-transporting protein 1S (RTP1S), and their localization in the plasma membrane was confirmed as previously described [62,63]. Transient transfection of ORs into Hana3A cells was performed with Lipofectamine 2000 (#11668-019; Thermo Fisher Scientific). Briefly, the transfected cells were grown on 22-mm coverslips (#0101050; Paul Marienfeld, Am Wöllerspfad, Germany) coated with poly-D-lysine ($10 \mu\text{g}\cdot\text{mL}^{-1}$; #P7280; Sigma-Aldrich). They were then washed with PBS and cooled on ice for 30 min to block endocytosis. Next, after washing in ice-cold PBS, the cells were fixed for 2 min in ice-cold methanol : acetone (v/v = 1 : 1) (methanol: Merck, #106009; acetone: Sigma-Aldrich, #179124). The cells were then incubated with 5% normal horse serum (#008-000-121; Jackson ImmunoResearch, W. Grove, PA, USA) in PBS for 1 h at room temperature. The sample was then incubated overnight at 4 °C with antirhodopsin or rabbit anti-Olfr110. After washing with PBS, Cy3-conjugated donkey anti-mouse antibody, Alexa488-conjugated donkey anti-mouse, or Cy3-conjugated donkey anti-rabbit was added and incubated for 1 h at RT in PBS containing 5% normal horse serum. The antibodies used are summarized in Table 5. Cells were mounted with Vectashield fluorescent mounting medium containing 4',6-diamidino-2-phenylindole (DAPI) (#H-1200; Vector Laboratories, Burlingame, CA, USA). Heterologous OR expression was analyzed on an LSM700 confocal laser scanning microscope, and image data were processed using the ZEN software (Zeiss, Oberkochen, Germany).

Luciferase assay

The Dual-Glo luciferase assay system (#E2940; Promega, Madison, WI, USA) was used for OR ligand screening as previously described [61]. Briefly, Hana3A cells were seeded in white polystyrene 96-well plates (#353296; BD Biosciences) 1 day before transfection. In each well, pCRELuc (#219076; Agilent Technologies, Santa Clara, CA, USA), pRL-SV40 (#E2231; Promega), RTP1S, and OR (or Mock) vectors were transfected for 24 h using Lipofectamine 2000 (#11668-019; Thermo Fisher Scientific). Transfected cells were stimulated at 37 °C for 4 h with various concentrations of odorants diluted in CD293 medium (#11913-019; Thermo Fisher Scientific). The activity of firefly luciferase

was normalized against that of *Renilla* luciferase. Luminescence was measured on a SpectraMax L microplate reader (Molecular Devices).

Homology modeling

Comparative homology modeling of mouse odorant receptors (ORs) Olfr110 and Olfr111, including template search, sequence alignment, model building, template selection, and model quality estimation, was conducted using the Web-based homology modeling tool SWISS-MODEL. The amino acid sequences of Olfr110 and Olfr111 were first obtained from National Center for Biotechnology Information (NCBI) Protein Basic Local Alignment Search Tool (BLAST) using the UniprotKB/Swiss-Prot database. Template searches for Olfr110 and Olfr111 with BLAST and HHblits were then performed against the SWISS-MODEL Template Library. A total of 179 and 186 templates were found for Olfr110 and Olfr111, respectively. The X-ray crystal structure of human adenosine A2A receptor [resolution: 2.7 Å, protein data bank (PDB) ID: 3VG9] was selected as the template structure for building the homology models of Olfr110 and Olfr111, based on both sequence identity and similarity. The 3D homology model structure built with the template alignment was generated using PROMOD (Ver 3.70, Swiss model server, Basel, Switzerland). The QMEAN scoring function was utilized for global and per-residue model quality assessment of the generated models. The final 3D model structures of Olfr110 and Olfr111 were downloaded from the SWISS-MODEL website. The results of comparative homology modeling of Olfr110 and Olfr111 were submitted to Protein Model DataBase (PMDb) with PMDB id, PM0082389, and are summarized in Table 4.

Receptor–ligand molecular docking

The 2D structures of the ligands were created by CHEMDRAW (ver. 11.0.1, PerkinElmer, Waltham, MA, USA) and transferred to CHEM3D PRO (ver. 11.0.1, PerkinElmer) to generate 3D structures. Ligand preparation and optimization were performed by the ‘Sanitize’ protocol (default) in SYBYL-X 2.1.1 (Tripos Inc., St. Louis, MO, USA) to clean up the 3D ligands by filling valences and removing duplicates. Homology models of Olfr110 and Olfr111 (template structure PDB ID: 3VG9) were then generated using the SWISS-MODEL homology modeling tool. The structure preparation tool in SYBYL-X 2.1.1 was used for protein preparation. Bumped side chains of amino acid residues were fixed, and all hydrogen atoms were added using the TRIPOS force field. Protein minimization was then performed by the POWELL method [64] with the following setup: The initial optimization set was changed to ‘None’ from the default setting SIMPLEX; the termination gradient was set to 0.5 kcal/(mol*Å); and the maximum iteration was set to 1000 times. Next, the entire docking process with prepared proteins and ligands was performed

using the Surflex-Dock GeomX module in SYBYL-X 2.1.1. The docking site was guided by the Surflex-Dock 'protomol', an idealized representation of a ligand that presents all potential interactions with binding site residues. The protomol was defined by selecting the largest receptor cavity from 'Multi-channel surface' mode in SYBYL-X 2.1.1. Two protomol generation factors, Bloat and Threshold, were set to 0.5 (Å) and 0, respectively. The maximum number of generated poses was set to 20. The minimum RMSD between the final poses was set to 0.05. Other docking parameters of Surflex-dock GeomX were set to the default values.

Site-directed mutagenesis

Site-directed mutants of the Olfr110 vector were generated as described in a previous study using *Pfu* Ultra High-Fidelity DNA polymerase (#600380; Agilent Technologies) [61]. All mutant vectors (F102W; F104W; Y252F; Y259F; F102W/F104W; Y252F/Y259F; F102W/Y252F/Y259F; F104W/Y252F/Y259F; F102W/F104W/Y252F/Y259F) were verified by both forward and reverse sequencing (Macrogen, Seoul, Korea).

Sample preparation

Synthetic 2-PF solution (purity > 98%) was purchased from Sigma-Aldrich. An equal volume of absolute (99.9%) methanol was added to the original solution. Both the original 2-PF solution (2-PF) and the solution to which methanol was added (2-PF + CH₃OH) were analyzed by direct infusion MS (Fig. 4A). For LC-MS/MS analysis of synthetic 2-PF, the 2-PF + CH₃OH solution was used (Fig. 4A,B). For LC-MS/MS analysis of Sup and THY media (Ctrl), Sup or Ctrl (1 mL) was filtered through an Ultracel YM-3 membrane with a pore size of 3 kD (Millipore Corporation) to remove proteins. Five hundred microliters of the FT was mixed with an equal volume of methanol. The resultant sample was sonicated for 10 min and centrifuged at 14 000 *g* at 4 °C for 20 min [65]. The Sup was analyzed by LC-MS/MS (Fig. 4C,D). In addition, 2-PF was added to Sup at a concentration of 0.1 or 10 mM, and the resultant sample was acidified with 0.1% trifluoroacetic acid and analyzed by LC-MS/MS (Fig. 4E).

Direct infusion with Heated Electrospray Ionization (HESI) source

2-PF and 2-PF + CH₃OH samples were injected at a flow rate of 20 μL·min⁻¹ using a 500-μL gas-tight syringe into the HESI source, and then measured for 8 min by the single-ion monitoring method on a Q-Exactive Hybrid Quadrupole-Orbitrap mass spectrometer (Thermo Fisher Scientific). The capillary voltage was set at 3.5 kV (positive mode), and the temperature of the desolvation capillary was set to 250 °C. The full mass spectrum was monitored

for the mass range between 50 and 750 Thompsons (Th) at a resolution of 70 000 (at *m/z* 200). Maximum ion injection time was 100 ms, with an automatic gain control value of 1×10^6 . The isolation window was set to *m/z* = 1.0 [66].

LC-MS/MS analysis

A Thermo EASY-nLC 1000 (Thermo Fisher Scientific) equipped with an analytical column (Thermo Fisher Scientific, Easy-Column, 75 μm × 50 cm), and a trap column (75 μm × 2 cm) was used for LC separation with the following parameters: injection volume = 10 μL; operation temperature of the analytical columns = 50 °C; flow rate = 300 nL·min⁻¹; mobile phase A = 0.1% formic acid; and mobile phase B = 0.1% formic acid and 2% water in acetonitrile. For LC separation, the following gradient was used: from 2% to 40% solvent B over 36 min, from 40% to 80% solvent B over 6 min, and from 80% to 2% solvent B over 6 min. The eluted samples from LC were analyzed on a Q-Exactive™ hybrid quadrupole-Orbitrap mass spectrometer (Thermo Fisher Scientific) equipped with a nanoelectrospray source. The capillary voltage was set to 3.5 kV (positive mode), and the temperature of the desolvation capillary was set to 250 °C. The Q-Exactive was operated in data-dependent mode, with survey scans acquired for the mass range between 50 and 750 Th at a resolution of 70 000 (at *m/z* 200). Up to the top 10 most abundant ions from the survey scan were selected with an isolation window of *m/z* = 1.0, and the ions were fragmented by higher-energy collisional dissociation with the normalized collision energies of 25 and exclusion duration of 10 s. MS/MS scans were acquired at a resolution of 17 500. Maximum ion injection times were 100 and 50 ms for full MS and MS/MS scans, respectively [67]. The automated gain control target value was set to 1.0×10^6 and 1.0×10^5 for full MS and MS/MS scans, respectively.

Extracted ion chromatogram (EIC) and MS/MS spectra

From each raw MS dataset containing full MS and MS/MS scans, the extracted ion chromatogram (EIC) for the 2-PF precursor ion with *m/z* = 153.091 Da was generated by extracting the chromatographic peaks within a tolerance of 2 p.p.m. For each fragmented peak (*m/z_f*) in MS/MS spectra of the 2-PF precursor ion, the candidate structure was obtained as that assigned to the corresponding fragmented peak with *m/z_f* minus the mass of CH₃ in the predicted MS/MS spectrum of 2-PF reported in the human metabolome database (HMDB) [68].

Immunofluorescence staining

For immunofluorescence staining, mouse primary MG were seeded on 22-mm coverslips (#0101050; Paul

Marienfeld) coated with poly-D-lysine (10 $\mu\text{g}\cdot\text{mL}^{-1}$; #P7280; Sigma-Aldrich) and incubated under standard conditions for 48 h. Cells were washed in PBS, fixed in 4% paraformaldehyde (#6148; Sigma-Aldrich) in PBS for 5 min, and blocked at room temperature for 1 h with PBS containing 4% normal horse serum (#008-000-121; Jackson ImmunoResearch) and 0.1% TWEEN[®] 20 (#P9416; Sigma-Aldrich). The cells were then incubated in blocking buffer at 4 °C overnight with primary antibodies (Table 5): Olfr110, Iba-1, and GFAP. Samples were then incubated at room temperature for 1 h in PBS containing 0.1% TWEEN[®] 20 (#P9416; Sigma-Aldrich) and secondary antibody: Cy3-conjugated donkey anti-rabbit, Alexa Fluor 488-conjugated donkey anti-goat, or Alexa Fluor 488-conjugated donkey anti-mouse. Cells were mounted with Vectashield fluorescent mounting medium, including DAPI (#H-1200; Vector Laboratories). Images were obtained using an LSM700 confocal laser scanning microscope and the ZEN software (Zeiss).

Immunohistochemistry

Mice were anesthetized with 400 mg ketamine per kg of body weight and transcardially perfused with PBS, followed by fixation with 4% paraformaldehyde (PFA; #6148; Sigma-Aldrich) in PBS. Brains were transferred into 4% PFA at 4 °C for 4 h, transferred to 30% sucrose in PBS for 1 day, cryo-preserved with O.C.T. compound (#4583; Scigen, Paramount, CA, USA), and sliced at a thickness of 30 μm using a cryotome (#HM 550; Thermo Fisher Scientific). Brain slices were placed on the slides, which were then blocked for 30 min in 2% normal donkey serum (#005-000-121; Jackson ImmunoResearch) in 0.3% PBST (1X PBS/0.3% Triton X-100) and incubated with primary antibodies (1 : 10 000 rabbit anti-Olfr110; 1 : 1000 goat anti-Iba-1; 1 : 1000 mouse anti-GFAP) in blocking buffer at 4 °C overnight. Slides were then incubated with secondary antibodies: Cy3-conjugated donkey anti-rabbit, Alexa Fluor 488-conjugated donkey anti-mouse, or Alexa Fluor 488-conjugated donkey anti-goat in PBST. Stained slices were mounted with Vectashield fluorescent mounting medium containing DAPI (#H-1200; Vector Laboratories). Immunostained images were obtained using an LSM700 confocal laser scanning microscope. Quantitative cell counting was performed as previously described [19].

Ex vivo phagocytosis analysis

The brain from a 9-week-old male CX3CR1^{GFP/+} mouse was sliced at a thickness of 150 μm on a vibratome (VT1200; Leica, Wetzlar, Germany) in ice-cold oxygenated artificial cerebrospinal fluid (aCSF; 120 mM NaCl, 25 mM NaHCO₃, 1.25 mM NaH₂PO₄, 5 mM KCl, 1 mM CaCl₂,

1 mM MgSO₄, and 305 mOsm with glucose, pH 7.4). To remove cellular debris, sliced brains were incubated in oxygenated aCSF at 37 °C for 2 h in the perfusion chamber, and then incubated with fresh aCSF (500 μl) containing 9.10×10^7 microspheres (360/407 nm; #17458; Polysciences, Warrington, PA, USA) and covered with a customized nylon grid. Before incubation, 500 μm 2-PF was added to fresh aCSF. Time-lapse movie clips were acquired at 1-min intervals for 92 min on a confocal microscope. Phagocytic beads and phagocytic MG were counted in the resultant images.

Knockdown and rescue experiments

Mouse primary MG were seeded in 6-well plates 1 day before transfection. Primary MG were then transfected for 24 h with *Olfr110* siRNA (#LQ-064350-01-0002; set of four ON-TARGET plus Mouse *Olfr110* siRNAs: #1: CCU GAAUUUAUACGCUAA; #2: CGUUAAGGUACU CAUUUAU; #3: CUGAAUGAAUUGCAGUAUU; #4: GAUUGAUCUCAGUGCUGUA; Dharmacon, Lafayette, CO, USA) or 100 nM nontarget siRNA (UGGUUUA-CAUGUCGACUAA, Thermo Fisher Scientific) in Opti-MEM (#11058021; Thermo Fisher Scientific) using Lipofectamine RNAiMAX (#13778150; Thermo Fisher Scientific). The efficiency of siRNA delivery to primary MG was confirmed using siGLO Red oligonucleotide duplex (#D-001630-02-05; Thermo Fisher Scientific). The siRNA #3 rescue vector for *Olfr110* containing several silent mutations (5'-CUCAACGAGCUGCAAUACC-3') was generated by site-directed mutagenesis as described above and then transfected for 24 h for *Olfr110* knockdown. For rescue experiments, the rescue vector was transfected for 24 h using Lipofectamine LTX (#15338100; Thermo Fisher Scientific) into cells previously transfected with nontarget or siRNA #3.

Ex vivo knockdown and rescue experiments

Nine-week-old male CX3CR1^{GFP/+} mice were anesthetized with ketamine. A small hole (~1 mm in diameter) was drilled into the skull, and a unilateral stereotaxic injection was performed to access the brain (bregma – 0.11 mm, 1 mm left from longitudinal fissure). Then, 0.5 μL siRNA (665 ng) and 0.5 μL siGLO Red oligonucleotide duplex (133 ng, #D-001630-02-05; Thermo Fisher Scientific) were combined and injected into the cerebral cortex in the presence of Mock vector (knockdown) or rescue vector (recovery) using Lipofectamine RNAiMAX. The stereotaxic injection was performed using a Hamilton syringe and infusion pump at a rate of 0.5 $\mu\text{L}\cdot\text{min}^{-1}$. At 48 h after injection, *ex vivo* imaging analysis was performed as previously described with slight modifications [33]. Delivery of siRNA and construct was confirmed by monitoring red

fluorescence from the siGLO Red oligonucleotide duplex. We also confirmed the efficiency of transfection by performing qRT-PCR of microdissected tissues at the injection site.

mRNA sequencing and data analysis

After treatment with vehicle (Control), Sup (MOI 100), or 2-PF (100 μM) for 2 h, total RNA was isolated from 2×10^6 cells of primary MG using the RNeasy mini Kit (74104; Qiagen, Hilden, Germany) and quantified using the Qubit RNA HS assay kit (Q32852; Thermo Fisher Scientific). The RNA integrity number of each sample was measured using the Agilent Technologies 2100 BioAnalyzer; RINs for all the samples were larger than 8.5, which is suitable for mRNA sequencing. Full-length cDNA was generated using the SMARTer-Seq v4 Ultra-Low Input RNA Kit for sequencing (#634888; Clontech, Mountain View, CA, USA). First-strand cDNA synthesis was initiated by adding 1 μL 3' SMART CDS primer II A to 10 ng total RNA and incubating at 72 °C for 3 min. Second strands were synthesized by adding SMARTer-seq v4 oligo and SMARTScribe reverse transcriptase, and the reaction was incubated at 42 °C for 90 min, followed by inactivation at 70 °C for 10 min. Double-stranded cDNA was amplified by PCR for 8 cycles and then purified using Agencourt AMPure beads (A63881; Beckman). mRNA-seq libraries were generated using the Nextera XT DNA library preparation kit (Illumina; FC-131-1024). cDNA was subjected to tagmentation (simultaneous fragmentation and tagging with sequencing adapters) and amplified by PCR using Index Primers from the Nextera XT DNA Index Kit (FC-131-1001; Illumina, San Diego, CA, USA). After PCR, the DNA library was purified using AMPure beads and quality was assessed using an Agilent 2100 Bioanalyzer. DNA libraries from individual samples were quantified using the KAPA Library Quantification kit (KK4854; KAPA Biosystems, Wilmington, MA, USA) and then pooled. All libraries were sequenced on an Illumina HiSeq2500 instrument to generate dual-indexed 100-bp paired reads, yielding an average of 58 million reads for each sample. After acquisition of read sequences for each sample, we checked the quality of raw sequences by FastQC (Babraham Bioinformatics) and trimmed the adapter sequences (TruSeq™ index adapter with the option '-a AGATCGGAAGAGCACACGTCTGAACTCCAGTCAC', and the reverse complement of TruSeq™ universal adapters with the option '-a AGATCGGAAGAGCGTCGTGTAGGGAAAGAGTGTGATCTCGGTGGTCGCCGTATCATT') using the cutadapt software. The remaining reads were then aligned to the mouse reference genome (GRCm38) using TopHat [69] with default parameters. We then assembled the aligned reads to annotated genes and calculated the fragments per kilobase per million mapped reads (FPKM) using Cufflinks [70].

Identification of differentially expressed genes

On average, 58 million reads were acquired from each sample, and 89.9% of the reads were aligned to the mouse reference genome. Genes with FPKM > 1 in at least one sample were considered to be expressed, as previously described [71]. After adding 1 to the FPKM values for the individual samples, we applied quantile normalization [72] to the \log_2 -converted FPKM values. Based on the normalized values, we performed the following comparisons to identify DEGs using an integrative statistical test reported previously [73]: Sup-treated samples vs. Control (Sup) and 2-PF-treated samples vs. Control (2-PF). For each gene, Student's *t*-test was performed to obtain a *T*-value. An empirical null distribution of the *T*-value was generated by performing random sampling experiments 1000 times and applying Gaussian kernel density estimation to *T*-values resulting from random sampling experiments. For each gene, the adjusted *P*-value for the observed *T*-value was calculated using the empirical distribution by the two-tailed test. DEGs were identified as the genes with an adjusted *P*-value < 0.05 and absolute \log_2 -median-ratio greater than a cutoff (\log_2 -fold change = 0.41 and 0.54 for Sup vs. Controls and 2-PF vs. Controls, respectively). The cutoff was determined as the average of the 5th and 95th percentile values in the distribution of \log_2 -fold changes obtained from the random sampling experiments described above. Enrichment analysis of GOBP was performed using the DAVID software [74].

cAMP ELISA

Primary MG were seeded in 48-well plates (2×10^5 cells/well) and treated for 30 min with vehicle, 30 μM forskolin (#F3917; Sigma-Aldrich), or 2-PF (10, 100, or 500 μM). To confirm the effect of inhibitor, the cells were pretreated with 1 mM SQ22536 (#17318-31-9; Calbiochem, San Diego, CA, USA) for 30 min. The cells were then lysed by incubation for 10 min in 0.1 M HCl containing 1% Triton X-100, and the lysate was centrifuged at $600 \times g$ for 2 min. The resultant supernatants were analyzed using the cAMP ELISA kit (Enzo Life Science, Farmingdale, NY, USA). Optical density at 405 nm was measured on a VersaMax microplate reader (Molecular Devices).

Calcium imaging

Twenty-four hours after freshly isolated MG were seeded on 18-mm round microscope cover glasses (#0111580; Paul Marienfeld) coated with poly-D-lysine, the cells were incubated in a superfusion chamber for 30 min with 4 μM Fura-2/AM (#F1221; Thermo Fisher Scientific) in Ringer's solution (115 mM NaCl, 2.5 mM KCl, 1 mM CaCl_2 , 1.5 mM MgCl_2 , 4.5 mM HEPES, pH 7.4) filtered through a membrane (0.22 μm pore size). After incubation with Ca^{2+} dye, the chamber was placed on the stage of an inverted microscope

(Eclipse Ti, Nikon, Tokyo, Japan) and washed with Ringer's solution for 20 min prior to 2-PF treatment. Ringer's solution was perfused at a flow rate of 12 mL·min⁻¹. First, the MG were treated with 300 μM ATP (#A2383; Sigma-Aldrich) for 5 s. After washing for 5 min, the cells were treated with 100 μM 2-PF. This step was conducted sequentially for two different concentrations of 2-PF (300 and 1000 μM). Finally, the cells were again treated with 300 μM ATP for 5 s. Emitted fluorescence was recorded every 2 s using a CCD camera (Andor Technology, Belfast, UK). Pseudocolor images were generated from fractional fluorescence changes ($\Delta F/F$, $\Delta [Ca^{2+}]_i$), which represent changes in the level of intracellular calcium. For movie clips, pseudocolor intensity was restricted to the maximum 1.5 ± 0.1 AU (arbitrary linear units) and a minimum of 0.4 ± 0.1 AU. The representative Ca²⁺ peak was selected after analysis of more than 160 cells.

Western blot

Cells were prepared using the T-PER[®] reagent (#78510; Thermo Fisher Scientific) with protease inhibitors (#04-693-116-001; Roche Molecular Diagnostics) and then lysed using MagNA Lyser (Roche Molecular Diagnostics). Total protein extract was quantified by Bradford assay. Samples were resolved by 7.5% SDS/PAGE or on 4–20% gradient Mini-PROTEAN TGX Precast Gels (#456-1064; Bio-Rad Laboratories, Hercules, CA, USA) and then blotted onto nitrocellulose membranes (#10600002; GE Healthcare, Chicago, IL, USA). The membranes were blocked for 1 h in 5% nonfat dry milk and TBST, 0.1% TWEEN[®] 20 (#P9416; Sigma-Aldrich), and Tris-buffered saline, and then incubated at 4 °C overnight with primary antibodies (Table 5): Immunoreactive protein bands were detected using SuperSignal[™] West Pico Chemiluminescent Substrate (#34080; Thermo Fisher Scientific) or SuperSignal[™] West Femto Maximum Sensitivity Substrate (#34095; Thermo Fisher Scientific).

Chemicals and inhibitors

Chemicals were purchased from Sigma-Aldrich except as noted. Acetic acid (#695092), acetone (#W332607), 2-aminoacetophenone (#W390607), dimethyl sulfide (#471577), ethanol (#E7023), hexanal (#115606), hydrogen sulfide (#742546), indole (#W259306), isopentanol (#320021), 2-PF (#W331708), trimethylamine (#W324108), furan (#185922), 2-methylfuran (#M46846), 2,3-dimethylfuran (#428469), 2-ethylfuran (#W367303), 2-propylfuran (#P1488; Tokyo Chemical Industry, Tokyo, Japan), 2-butylfuran (#CDS001204), 2-*t*-butylfuran (#386278), 2-hexylfuran (#H26698; Alfa Aesar, Ward Hill, MA, USA), and 2-heptylfuran (#A10604; Alfa Aesar) were diluted in DMSO (#D2650). ATP (#A2383) was diluted in distilled water, and LPS (#L2630) was diluted in DMSO. Inhibitors of AC, PKA, ERK, G_{βγ}, and PLC-β were diluted with DMSO and used at the following concentrations: 50 μM for PD98059 (#PHZ1164; Thermo Fisher Scientific),

300 μM for SQ22536 (#568500; Calbiochem), 5 μM for U73122 (#662035; Calbiochem), 10 μM for H-89 (#tlrl-h89; InvivoGen, San Diego, CA, USA), and 10 μM for gallein (#371709; Calbiochem). Cells were pretreated with each inhibitor for 1 h prior to experiments.

Statistical analyses

All data are shown as means ± SEM. Statistical significance was determined by unpaired Student's *t*-test for comparisons of repeated measurements and their respective control values. Analyses were performed in the PRISM 5 Software (GraphPad Software, San Diego, CA, USA).

Acknowledgements

This work was supported by grants from the Korean Mouse Phenotype Center (2019M3A9D5A01000073) and the National Research Foundation (2019R1H1A2100811).

Conflict of interest

The authors declare no conflict of interest.

Author contributions

JK and DH designed and directed the project. NL, YJ, YRH, and JK performed primary cell culture, bacterial culture, qRT-PCR, IHC, western blots, cytokine ELISA, chemotaxis, phagocytosis assays, ROS measurements, cloning, luciferase assays, knockdown and rescue experiments, and cAMP ELISAs. NL, HK, KK, YB, and JK performed homology modeling and site-directed mutagenesis experiments. NL, SC, SA, JHJ, DH, and JK performed proteomic experiments and data analyses. YJ, NL, TC, CL, JS, JB, and JK performed IHC, *in situ* hybridization, *ex vivo* phagocytosis analysis, *ex vivo* knockdown and rescue experiments, and calcium imaging. NL, MK, DYH, DH, and JK performed genomic experiments and data analyses. JK, DH, NL, YB, YJ, MK., DYH, and SA wrote the manuscript.

References

- Hanisch UK & Kettenmann H (2007) Microglia: active sensor and versatile effector cells in the normal and pathologic brain. *Nat Neurosci.* **10**, 1387–1394.
- Nimmerjahn A, Kirchhoff F & Helmchen F (2005) Resting microglial cells are highly dynamic surveillants of brain parenchyma *in vivo*. *Science* **308**, 1314–1318.
- Kreutzberg GW (1996) Microglia: a sensor for pathological events in the CNS. *Trends Neurosci* **19**, 312–318.

- 4 Block ML, Zecca L & Hong JS (2007) Microglia-mediated neurotoxicity: uncovering the molecular mechanisms. *Nat Rev Neurosci* **8**, 57–69.
- 5 Rock RB, Gekker G, Hu S, Sheng WS, Cheeran M, Lokensgard JR & Peterson PK (2004) Role of microglia in central nervous system infections. *Clin Microbiol Rev* **17**, 942–964, table of contents.
- 6 Mook-Kanamori BB, Geldhoff M, van der Poll T & van de Beek D (2011) Pathogenesis and pathophysiology of pneumococcal meningitis. *Clin Microbiol Rev* **24**, 557–591.
- 7 Braun JS, Sublett JE, Freyer D, Mitchell TJ, Cleveland JL, Tuomanen EI & Weber JR (2002) Pneumococcal pneumolysin and H₂O₂ mediate brain cell apoptosis during meningitis. *J Clin Invest* **109**, 19–27.
- 8 Kim JY, Paton JC, Briles DE, Rhee DK & Pyo S (2015) *Streptococcus pneumoniae* induces pyroptosis through the regulation of autophagy in murine microglia. *Oncotarget* **6**, 44161–44178.
- 9 Peppoloni S, Colombari B, Neglia R, Quaglino D, Iannelli F, Oggioni MR, Pozzi G & Blasi E (2006) The lack of Pneumococcal surface protein C (PspC) increases the susceptibility of *Streptococcus pneumoniae* to the killing by microglia. *Med Microbiol Immunol* **195**, 21–28.
- 10 Hanisch UK, Prinz M, Angstwurm K, Hausler KG, Kann O, Kettenmann H & Weber JR (2001) The protein tyrosine kinase inhibitor AG126 prevents the massive microglial cytokine induction by pneumococcal cell walls. *Eur J Immunol* **31**, 2104–2115.
- 11 Bjarnadottir TK, Gloriam DE, Hellstrand SH, Kristiansson H, Fredriksson R & Schiöth HB (2006) Comprehensive repertoire and phylogenetic analysis of the G protein-coupled receptors in human and mouse. *Genomics* **88**, 263–273.
- 12 Hickman SE, Kingery ND, Ohsumi TK, Borowsky ML, Wang LC, Means TK & El Khoury J (2013) The microglial sensome revealed by direct RNA sequencing. *Nat Neurosci* **16**, 1896–1905.
- 13 McHugh D (2012) GPR18 in microglia: implications for the CNS and endocannabinoid system signalling. *Br J Pharmacol* **167**, 1575–1582.
- 14 Pietr M, Kozela E, Levy R, Rimmerman N, Lin YH, Stella N, Vogel Z & Juknat A (2009) Differential changes in GPR55 during microglial cell activation. *FEBS Lett* **583**, 2071–2076.
- 15 Gong JP, Onaivi ES, Ishiguro H, Liu QR, Tagliaferro PA, Brusco A & Uhl GR (2006) Cannabinoid CB2 receptors: immunohistochemical localization in rat brain. *Brain Res* **1071**, 10–23.
- 16 Pluznick JL, Protzko RJ, Gevorgyan H, Peterlin Z, Sipos A, Han J, Brunet I, Wan LX, Rey F, Wang T *et al.* (2013) Olfactory receptor responding to gut microbiota-derived signals plays a role in renin secretion and blood pressure regulation. *Proc Natl Acad Sci USA* **110**, 4410–4415.
- 17 Kang N & Koo J (2012) Olfactory receptors in non-chemosensory tissues. *BMB Rep* **45**, 612–622.
- 18 Massberg D & Hatt H (2018) Human olfactory receptors: novel cellular functions outside of the nose. *Physiol Rev* **98**, 1739–1763.
- 19 Kang N, Kim H, Jae Y, Lee N, Ku CR, Margolis F, Lee EJ, Bahk YY, Kim MS & Koo J (2015) Olfactory marker protein expression is an indicator of olfactory receptor-associated events in non-olfactory tissues. *PLoS ONE* **10**, e0116097.
- 20 Busse D, Kudella P, Gruning NM, Gisselmann G, Stander S, Luger T, Jacobsen F, Steinstrasser L, Paus R, Gkogkolou P *et al.* (2014) A synthetic sandalwood odorant induces wound-healing processes in human keratinocytes via the olfactory receptor OR2AT4. *J Invest Dermatol* **134**, 2823–2832.
- 21 Flegel C, Manteniotis S, Osthold S, Hatt H & Gisselmann G (2013) Expression profile of ectopic olfactory receptors determined by deep sequencing. *PLoS ONE* **8**, e55368.
- 22 Di Pizio A, Behrens M & Krautwurst D (2019) Beyond the flavour: the potential druggability of chemosensory G protein-coupled receptors. *Int J Mol Sci* **20**, pii: E14 02. <https://doi.org/10.3390/ijms20061402>
- 23 Ferrer I, Garcia-Esparcia P, Carmona M, Carro E, Aronica E, Kovacs GG, Grison A & Gustincich S (2016) Olfactory receptors in non-chemosensory organs: the nervous system in health and disease. *Front Aging Neurosci* **8**, 163.
- 24 Ansoleaga B, Garcia-Esparcia P, Pinacho R, Haro JM, Ramos B & Ferrer I (2015) Decrease in olfactory and taste receptor expression in the dorsolateral prefrontal cortex in chronic schizophrenia. *J Psychiatr Res* **60**, 109–116.
- 25 Ansoleaga B, Garcia-Esparcia P, Llorens F, Moreno J, Aso E & Ferrer I (2013) Dysregulation of brain olfactory and taste receptors in AD, PSP and CJD, and AD-related model. *Neuroscience* **248**, 369–382.
- 26 Gaudel F, Stephan D, Landel V, Sicard G, Feron F & Guiraudie-Capraz G (2019) Expression of the cerebral olfactory receptors Olfr110/111 and Olfr544 Is altered during aging and in Alzheimer's disease-like mice. *Mol Neurobiol* **56**, 2057–2072.
- 27 Grison A, Zucchelli S, Urzi A, Zamparo I, Lazarevic D, Pascarella G, Roncaglia P, Giorgetti A, Garcia-Esparcia P, Vlachouli C *et al.* (2014) Mesencephalic dopaminergic neurons express a repertoire of olfactory receptors and respond to odorant-like molecules. *BMC Genom* **15**, 729.
- 28 Norden DM, Trojanowski PJ, Villanueva E, Navarro E & Godbout JP (2016) Sequential activation of microglia and astrocyte cytokine expression precedes increased Iba-1 or GFAP immunoreactivity following systemic immune challenge. *Glia* **64**, 300–316.

- 29 de March CA, Yu Y, Ni MJ, Adipietro KA, Matsunami H, Ma M & Golebiowski J (2015) Conserved residues control activation of mammalian G protein-coupled odorant receptors. *J Am Chem Soc* **137**, 8611–8616.
- 30 Cong X, Topin J & Golebiowski J (2017) Class A GPCRs: structure, function, modeling and structure-based ligand design. *Curr Pharm Des* **23**, 4390–4409.
- 31 Zhang Y, Chen K, Sloan SA, Bennett ML, Scholze AR, O’Keeffe S, Phatnani HP, Guarnieri P, Caneda C, Ruderisch N *et al.* (2014) An RNA-sequencing transcriptome and splicing database of glia, neurons, and vascular cells of the cerebral cortex. *J Neurosci* **34**, 11929–11947.
- 32 Wornle M, Schmid H, Banas B, Merkle M, Henger A, Roeder M, Blattner S, Bock E, Kretzler M, Grone HJ *et al.* (2006) Novel role of toll-like receptor 3 in hepatitis C-associated glomerulonephritis. *Am J Pathol* **168**, 370–385.
- 33 Takayama F, Hayashi Y, Wu Z, Liu Y & Nakanishi H (2016) Diurnal dynamic behavior of microglia in response to infected bacteria through the UDP-P2Y6 receptor system. *Sci Rep* **6**, 30006.
- 34 Verderio C & Matteoli M (2001) ATP mediates calcium signaling between astrocytes and microglial cells: modulation by IFN-gamma. *J Immunol* **166**, 6383–6391.
- 35 Ukhanov K, Brunert D, Corey EA & Ache BW (2011) Phosphoinositide 3-kinase-dependent antagonism in mammalian olfactory receptor neurons. *J Neurosci* **31**, 273–280.
- 36 Bonacci TM, Mathews JL, Yuan C, Lehmann DM, Malik S, Wu D, Font JL, Bidlack JM & Smrcka AV (2006) Differential targeting of Gbetagamma-subunit signaling with small molecules. *Science* **312**, 443–446.
- 37 Marjonon H, Sierra A, Nyman A, Rogojin V, Grohn O, Linden AM, Hautaniemi S & Kaminen-Ahola N (2015) Early maternal alcohol consumption alters hippocampal DNA methylation, gene expression and volume in a mouse model. *PLoS ONE* **10**, e0124931.
- 38 Schaum N, Karkanias J, Neff NF, May AP, Quake SR, Wyss-Coray T, Darmanis S, Batson J, Botvinnik O & Chen MB *et al.* (2018) Single-cell transcriptomics of 20 mouse organs creates a *Tabula Muris*. *Nature* **562**, 367–372.
- 39 Zhuang H & Matsunami H (2007) Synergism of accessory factors in functional expression of mammalian odorant receptors. *J Biol Chem* **282**, 15284–15293.
- 40 Nagashima A & Touhara K (2010) Enzymatic conversion of odorants in nasal mucus affects olfactory glomerular activation patterns and odor perception. *J Neurosci* **30**, 16391–16398.
- 41 Pevsner J, Hou V, Snowman AM & Snyder SH (1990) Odorant-binding protein. Characterization of ligand binding. *J Biol Chem* **265**, 6118–6125.
- 42 Flower DR (1996) The lipocalin protein family: structure and function. *Biochem J* **318** (Pt 1), 1–14.
- 43 Wu C, Hwang SH, Jia Y, Choi J, Kim YJ, Choi D, Pathiraja D, Choi IG, Koo SH & Lee SJ (2017) Olfactory receptor 544 reduces adiposity by steering fuel preference toward fats. *J Clin Invest* **127**, 4118–4123.
- 44 Chang AJ, Ortega FE, Riegler J, Madison DV & Krasnow MA (2015) Oxygen regulation of breathing through an olfactory receptor activated by lactate. *Nature* **527**, 240–244.
- 45 Shepard BD, Koepsell H & Pluznick JL (2019) Renal olfactory receptor 1393 contributes to the progression of type 2 diabetes in a diet-induced obesity model. *Am J Physiol Renal Physiol* **316**, F372–f381.
- 46 Garcia-Esparcia P, Schluter A, Carmona M, Moreno J, Ansoleaga B, Torrejon-Escribano B, Gustincich S, Pujol A & Ferrer I (2013) Functional genomics reveals dysregulation of cortical olfactory receptors in Parkinson disease: novel putative chemoreceptors in the human brain. *J Neuropathol Exp Neurol* **72**, 524–539.
- 47 Lee SJ, Depoortere I & Hatt H (2019) Therapeutic potential of ectopic olfactory and taste receptors. *Nat Rev Drug Discov* **18**, 116–138.
- 48 Filipiak W, Beer R, Sponring A, Filipiak A, Ager C, Schiefecker A, Lanthaler S, Helbok R, Nagl M, Troppmair J *et al.* (2015) Breath analysis for *in vivo* detection of pathogens related to ventilator-associated pneumonia in intensive care patients: a prospective pilot study. *J Breath Res* **9**, 016004.
- 49 Syhre M, Scotter JM & Chambers ST (2008) Investigation into the production of 2-Pentylfuran by *Aspergillus fumigatus* and other respiratory pathogens *in vitro* and human breath samples. *Med Mycol* **46**, 209–215.
- 50 Barichello T, Generoso JS, Simoes LR, Goularte JA, Petronilho F, Saigal P, Badawy M & Quevedo J (2016) Role of microglial activation in the pathophysiology of bacterial meningitis. *Mol Neurobiol* **53**, 1770–1781.
- 51 Jung S, Aliberti J, Graemmel P, Sunshine MJ, Kreutzberg GW, Sher A & Littman DR (2000) Analysis of fractalkine receptor CX(3)CR1 function by targeted deletion and green fluorescent protein reporter gene insertion. *Mol Cell Biol* **20**, 4106–4114.
- 52 Cho T, Lee C, Lee N, Hong YR & Koo J (2019) Small-chain fatty acid activates astrocytic odorant receptor Olfr920. *Biochem Biophys Res Commun* **510**, 383–387.
- 53 Lee N, Sa M, Hong YR, Lee CJ & Koo J (2018) Fatty acid increases cAMP-dependent lactate and MAO-B-dependent GABA production in mouse astrocytes by activating a Galphas protein-coupled receptor. *Exp Neurobiol* **27**, 365–376.

- 54 Livak KJ & Schmittgen TD (2001) Analysis of relative gene expression data using real-time quantitative PCR and the 2(-Delta Delta C(T)) Method. *Methods* **25**, 402–408.
- 55 Kim H, Kang N, Chon KW, Kim S, Lee N, Koo J & Kim MS (2015) MRPrimer: a MapReduce-based method for the thorough design of valid and ranked primers for PCR. *Nucleic Acids Res* **43**, e130.
- 56 Kim H, Kang N, An K, Koo J & Kim MS (2016) MRPrimerW: a tool for rapid design of valid high-quality primers for multiple target qPCR experiments. *Nucleic Acids Res* **44**, W259–W266.
- 57 Babior BM, Kipnes RS & Curnutte JT (1973) Biological defense mechanisms. The production by leukocytes of superoxide, a potential bactericidal agent. *J Clin Invest* **52**, 741–744.
- 58 Yokomizo T, Izumi T, Chang K, Takuwa Y & Shimizu T (1997) A G-protein-coupled receptor for leukotriene B4 that mediates chemotaxis. *Nature* **387**, 620–624.
- 59 Bae YS, Bae H, Kim Y, Lee TG, Suh PG & Ryu SH (2001) Identification of novel chemoattractant peptides for human leukocytes. *Blood* **97**, 2854–2862.
- 60 Shepard BD, Natarajan N, Protzko RJ, Acres OW & Pluznick JL (2013) A cleavable N-terminal signal peptide promotes widespread olfactory receptor surface expression in HEK293T cells. *PLoS ONE* **8**, e68758.
- 61 Park BB, Lee N, Kim Y, Jae Y, Choi S, Kang N, Hong YR, Ok K, Cho J, Jeon YH *et al.* (2017) Analogues of dehydroacetic acid as selective and potent agonists of an ectopic odorant receptor through a combination of hydrophilic and hydrophobic interactions. *ChemMedChem* **12**, 477–482.
- 62 Behrens M, Brockhoff A, Batram C, Kuhn C, Appendino G & Meyerhof W (2009) The human bitter taste receptor hTAS2R50 is activated by the two natural bitter terpenoids andrographolide and amarogentin. *J Agric Food Chem* **57**, 9860–9866.
- 63 Zhuang H & Matsunami H (2008) Evaluating cell-surface expression and measuring activation of mammalian odorant receptors in heterologous cells. *Nat Protoc* **3**, 1402–1413.
- 64 Abagyan R, Totrov M & Kuznetsov D (1994) ICM—a new method for protein modeling and design: applications to docking and structure prediction from the distorted native conformation. *J Comput Chem* **15**, 488–506.
- 65 Lau SK, Lam CW, Curreem SO, Lee KC, Lau CC, Chow WN, Ngan AH, To KK, Chan JF, Hung IF *et al.* (2015) Identification of specific metabolites in culture supernatant of *Mycobacterium tuberculosis* using metabolomics: exploration of potential biomarkers. *Emerg Microbes Infect* **4**, e6.
- 66 Looße C, Galozzi S, Debor L, Julsing MK, Bühler B, Schmid A, Barkovits K, Müller T & Marcus K (2015) Direct infusion-SIM as fast and robust method for absolute protein quantification in complex samples. *EuPA Open Proteomics* **7**, 20–26.
- 67 Saigusa D, Okamura Y, Motoike IN, Katoh Y, Kurosawa Y, Saijyo R, Koshiba S, Yasuda J, Motohashi H, Sugawara J *et al.* (2016) Establishment of protocols for global metabolomics by LC-MS for biomarker discovery. *PLoS ONE* **11**, e0160555.
- 68 Wishart DS, Tzur D, Knox C, Eisner R, Guo AC, Young N, Cheng D, Jewell K, Arndt D, Sawhney S *et al.* (2007) HMDB: the human metabolome database. *Nucleic Acids Res* **35**, D521–D526.
- 69 Trapnell C, Pachter L & Salzberg SL (2009) TopHat: discovering splice junctions with RNA-Seq. *Bioinformatics* **25**, 1105–11011.
- 70 Trapnell C, Williams BA, Pertea G, Mortazavi A, Kwan G, van Baren MJ, Salzberg SL, Wold BJ & Pachter L (2010) Transcript assembly and quantification by RNA-Seq reveals unannotated transcripts. *Nat Biotechnol* **28**, 511–515.
- 71 Graveley BR, Brooks AN, Carlson JW, Duff MO, Landolin JM, Yang L, Artieri CG, van Baren MJ, Boley N, Booth BW *et al.* (2011) The developmental transcriptome of *Drosophila melanogaster*. *Nature* **471**, 473–479.
- 72 Bolstad BM, Irizarry RA, Astrand M & Speed TP (2003) A comparison of normalization methods for high density oligonucleotide array data. *Bioinformatics* **19**, 185–193.
- 73 Lee HJ, Suk JE, Patrick C, Bae E-J, Cho J-H, Rho S, Hwang D, Masliah E & Lee S-J (2010) Direct transfer of alpha-synuclein from neuron to astroglia causes inflammatory. *J Biol Chem* **285**, 9262–9272.
- 74 da Huang W, Sherman BT & Lempicki RA (2009) Systematic and integrative analysis of large gene lists using DAVID. *Nat Protoc* **4**, 44–57.
- 75 Filipiak W, Sponring A, Baur MM, Ager C, Filipiak A, Wiesenhofer H, Nagl M, Troppmair J & Amann A (2012) Characterization of volatile metabolites taken up by or released from *Streptococcus pneumoniae* and *Haemophilus influenzae* by using GC-MS. *Microbiology* **158**, 3044–3053.
- 76 Julak J, Stranska E, Prochazkova-Francisci E & Rosova V (2000) Blood cultures evaluation by gas chromatography of volatile fatty acids. *Med Sci Monit* **6**, 605–610.
- 77 Allardyce RA, Hill AL & Murdoch DR (2006) The rapid evaluation of bacterial growth and antibiotic susceptibility in blood cultures by selected ion flow tube mass spectrometry. *Diagn Microbiol Infect Dis* **55**, 255–261.
- 78 Scotter JM, Allardyce RA, Langford VS, Hill A & Murdoch DR (2006) The rapid evaluation of bacterial growth in blood cultures by selected ion flow tube-mass spectrometry (SIFT-MS) and comparison with the

BacT/ALERT automated blood culture system.
J Microbiol Methods **65**, 628–631.

Supporting information

Additional supporting information may be found online in the Supporting Information section at the end of the article.

Table S1. Genes affected by Sup and 2-PF.

Video S1. The phagocytic process (related to Fig. 6).

Video S2. Intracellular calcium response of primary microglia (related to Fig. 10).